Geophys. J. Int. (2007) **169,** 988–1008 doi: 10.1111/j.1365-246X.2006.03318.x

Fault slip in the 1997 Manyi, Tibet earthquake from linear elastic modelling of InSAR displacements

Gareth J. Funning,* Barry Parsons and Tim J. Wright†

COMET, Department of Earth Sciences, University of Oxford, Parks Road, Oxford OX1 3PR, *UK. E-mail: garethf@earth.ox.ac.uk*

Accepted 2006 December 3. Received 2006 November 30; in original form 2006 May 29

SUMMARY

The M_w 7.6 1997 Manyi earthquake occurred in an area of central northern Tibet where sparse vegetation coverage and a lack of human habitation provide excellent conditions for Interferometric Synthetic Aperture Radar (InSAR) studies. We use coseismic pairs of radar images acquired by the ESA ERS-2 satellite to construct interferograms of the surface displacement field due to the earthquake. The location and extent of the coseismic fault rupture are mapped using a combination of optical satellite imagery, high-resolution digital topography, interferometric correlation and azimuth offset measurements; in so doing, we are able to relate prominent geomorphic features in the fault zone to bends in the fault.

Using elastic dislocation models consistent with this mapped fault trace, we then test a range of fault geometries and slip conditions to find the combination which best explains the InSAR displacements. Our favoured model contains a reversal in fault dip, approximately halfway along its length, occurring at the location of a restraining bend. Slip on this model fault is heterogeneous, with two areas of peak slip of 7 m or greater, and components of dip-slip displacement which vary significantly along-strike. The success of this model in fitting the data implies that an observed asymmetry in the coseismic interferograms can be explained in terms of the local fault geometry, rather than by using non-linear elastic rheologies as suggested by earlier authors.

Key words: earthquake, elastic dislocation, InSAR, modelling, rheology, Tibet.

1 INTRODUCTION

On 1997 November 8, a M_w 7.5–7.6 earthquake struck the Manyi region of north central Tibet. This remote and uninhabited area, several hundred kilometres from the nearest major road, is very difficult, if not impossible, to access for field-based study, and so remote sensing techniques such as Interferometric Synthetic Aperture Radar (InSAR) constitute the best means available to learn about the deformation that occurred at the surface. Indeed, given the high modal elevation of the Manyi region (∼5000 m) and the corresponding lack of boreal vegetation, as well as the absence of human modification of the surface (e.g. agriculture), conditions on the ground here favour the application of InSAR. In this study, we use a high-resolution ground displacement data set obtained using InSAR, together with a map of the surface expression of the Manyi fault obtained using a combination of remote-sensing data sets, to invert for both the geometry and distribution of slip of the fault responsible. In so doing, we aim to address a recent controversy surrounding the nature of the elastic rheology operating in the upper crust in this area.

1.1 Tectonic setting

Among the striking surface tectonic features in northern Tibet are the large strike-slip faults which extend for hundreds of kilometres both along the edges and in the interior of the plateau. The largest of these interior strike-slip belts, the Kunlun fault zone, extends for over 1000 km in NE Tibet, and has an estimated left-lateral slip rate of ∼12 mm yr^{-1}, obtained by dating offset Quaternary features (Van der Woerd *et al.* 1998, 2002). The Kunlun fault is known to release strain in large earthquakes at its western end; in 2001, a M_w 7.8 earthquake occurred at Kokoxili (Fig. 1), rupturing approximately 450 km of the fault in three subevents (Xu *et al.* 2002; Antolik *et al.* 2004).

At its western end, the Kunlun fault is thought to split into a number of splays, which have been identified by interpretation of satellite images (Tapponnier & Molnar 1977), but have not been mapped extensively in the field. The Manyi fault, first identified by Tapponnier & Molnar (1977) is one of these splays, and has a trend almost continuous with that of the Kunlun fault. It is located some 200 km to the west along-strike from the Kunlun fault, and extends a further 200 km with this trend. The Manyi area has experienced two major earthquakes in the past four decades—the

*Now at: Berkeley Seismological Laboratory, University of California, Berkeley, CA 94720, USA.

†Now at: School of Earth and the Environment, University of Leeds, Leeds LS2 9JT, UK.

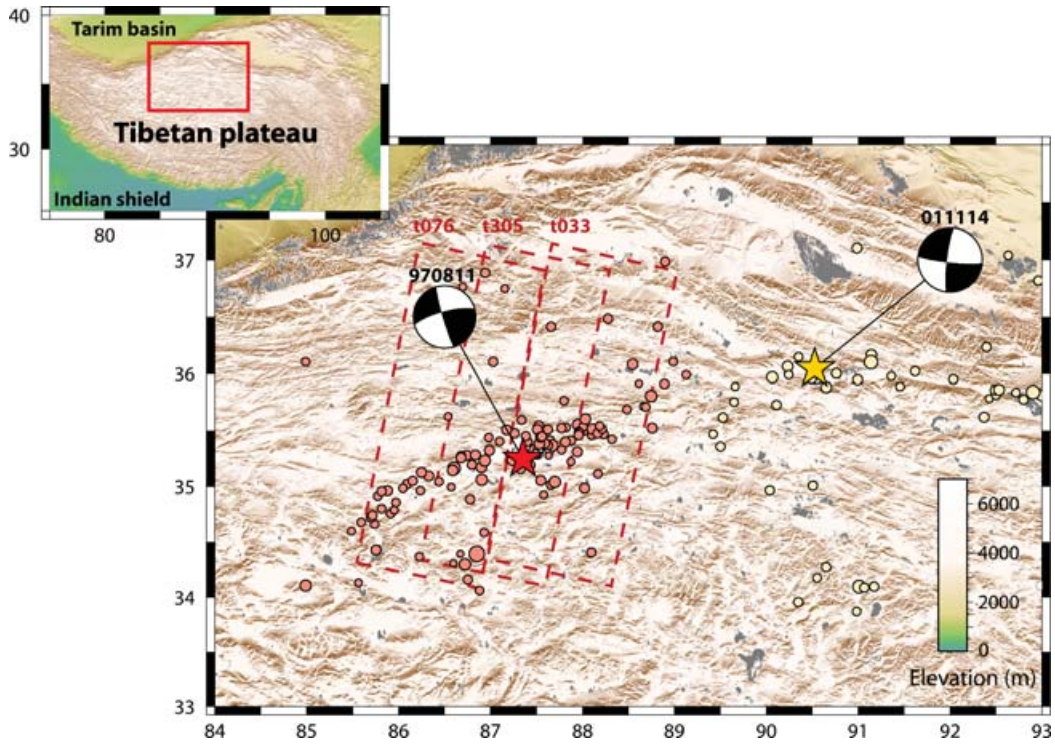

Figure 1. Location and seismicity map of the Manyi region. Red star shows main shock epicentre of the 1997 November 8 Manyi earthquake; pale red circles are aftershocks of this event. Main shock and aftershocks for the 2001 November 14 Kokoxili earthquake are marked with a gold star and pale yellow circles, respectively. Main shock focal mechanisms shown are from Velasco *et al.* (2000) and Antolik *et al.* (2004), respectively. In both cases, an approximately linear trend can be identified in the aftershocks parallel to one of the earthquake nodal planes, giving an indication of the location of the active fault responsible. Although not colinear, the two seismicity bands are almost continuous, suggesting a connection between the two faults. All events were located using joint hypocentral determination (Dewey 1971) relative to the Manyi hypocentre of Steck *et al.* (2001) by Robinson (private communication, 2005). Red dashed lines indicate the coverage of the three ERS–SAR tracks used in this study (track numbers are given). Topographic data are taken from the Shuttle Radar Topography Mission (SRTM; Farr & Kobrick 2000).

Table 1. Catalogued and published seismic solutions for the mechanism of the Manyi earthquake.

	Latitude	Longitude	Depth (km)	Strike	Dip	Rake	M_0 (N m)
Harvard CMT	35.33	86.96	16.4	79	69	2	2.23×10^{20}
NEIC	35.069	87.325	38.0	70	89	2	1.40×10^{20}
Velasco *et al.* (2000)	35.246	87.351	12	255	76	−5	1.80×10^{20}

M_w 7.4 1973 July 14 event, which had an oblique (strike-slip and normal) faulting mechanism (Molnar & Chen 1983) and was probably located at the western end of the identified Manyi fault (Tapponnier & Molnar 1977), and the 1997 earthquake which is the subject of this study.

1.2 Seismological observations of the Manyi earthquake

Catalogued and published seismic solutions (Velasco *et al.* 2000; Table 1; Fig. 1) for the 1997 Manyi earthquake are consistent with approximately E–W-striking left-lateral strike-slip faulting. Relocated aftershock data using regional velocity models (Velasco *et al.* 2000; Steck *et al.* 2001) delimit a fault zone – 200 km long, aligned with the previously identified Manyi fault (Tapponnier & Molnar 1977). Surprisingly, this large earthquake had no large aftershocks – the largest aftershock, a M_w 5.1 event, was around three orders of magnitude smaller than the main shock in moment.

In order to obtain a suite of solutions for the mechanism of the Manyi earthquake, Velasco *et al.* (2000) used a number of different seismological approaches, including surface wave spectral methods, inversion of body waves, aftershock relocation and empirical Green's function analysis. In general, their solutions had similar features, with seismic moments clustered around 2×10^{20} N m, values of rake consistent with almost pure left-lateral strike-slip motion on an E–W fault, and moment release occurring at depths of 15 km or shallower. Their body wave analysis suggested that the rupture propagated for around 50 s, bilaterally for the first 20 s and then westward for the remainder, with the observed *P*- and *SH*-wave radiation patterns explicable in terms of five subevents, all located within ∼25 km of the hypocentre.

1.3 Other studies of the Manyi earthquake

Peltzer *et al.* (1999) used synthetic aperture radar (SAR) data from the European Space Agency ERS-2 satellite to study the displacement field at the surface due to the earthquake, constructing interferograms and azimuth offsets. They interpreted an offset of the peak displacements observed on opposite sides of the fault as

representing the effects of a non-linear elastic rheology in the crust in this location, with a smaller elastic modulus operating when the crust is under tension than when under compression. The rationale for this was that the presence of pre-existing weaknesses, such as cracks, in the crust would act to limit its tensile strength. They calculated two models of the deformation—the first a linear elastic model, based on 7 m of pure left-lateral strike-slip on an 8-km-wide vertical fault, and the second a distributed-slip model, based on a 100 × 15 km fault, where different elastic moduli were tried in the compressional and dilatational quadrants of the deformation pattern. The former model did not match profiles of deformation taken across the fault; however, the latter models did match profiles taken along the fault, when the compressional and dilatational elastic moduli differed by a factor of two. On the basis of this, they asserted that non-linear elasticity is a plausible explanation for the deformation pattern.

This interpretation remains controversial (e.g. Fialko *et al.* 2001; Simons *et al.* 2002), however, as all other published models of large earthquakes generated from InSAR data, both prior and subsequent to this one have been adequately explained through the application of linear elastic theory. In this paper, we search for models that do not require non-linear elasticity, but rather explain the observed features of the interferograms in terms of the geometry of the fault.

2 MEASURING GROUND DISPLACEMENTS WITH INSAR

The rupture area of the Manyi fault, as defined by the aftershock zone, is covered by three ERS–SAR tracks (Fig. 1). Pairs of SAR images, covering three frames from each of these tracks and straddling the fault, were processed using the JPL/Caltech ROI_PAC software (Rosen *et al.* 2004). Details of the data used are given in Table 2. A 3 arcsec digital elevation model (DEM) obtained by the Shuttle Radar Topography Mission (hereafter SRTM; Farr & Kobrick 2000) was used for geocoding and to correct for any topographic signal in the data. Delft precise orbits (Scharroo & Visser 1998) were used to correct for the orbital contribution to phase. Given the size of the coseismic signal (see below) we prefer not to risk introducing systematic biases into our data by re-estimating the best planar or quadratic orbital correction during processing, preferring instead to estimate a correction when modelling the fault slip (Section 4). We unwrap the interferograms using the branch-cut unwrapper in ROI_PAC (e.g. Rosen *et al.* 2000); for the central track (track 305) interferogram, which is effectively cut into two halves by decorrelation, we unwrap each half separately and solve for a separate zero-level ambiguity for each during modelling.

The completed interferograms, rewrapped at 10 cm intervals, are shown in Fig. 2. The most prominent feature in the data is a large cluster of fringes, centred on the central track (track 305), representing the area of greatest moment release. There is a narrow, linear band of decorrelation that bisects this deformation pattern, cutting through the area of the highest deformation gradients, which is most probably due to the rupturing of the surface during the earthquake, and when compared with other satellite and topographic data, is interpreted as representing the surface trace of the coseismic fault (Section 3). The maximum peak-to-trough line-of-sight (LOS) offset observed across this feature is ∼2.4 m in the central and eastern tracks, which, if resolved into a purely horizontal motion along the trend of the surface rupture, is equivalent to a surface offset of ∼7 m.

This main deformation feature, when examined more closely, is demonstrably asymmetric. There is around 30 cm more LOS deformation to the south of the decorrelated band, than to the north, suggesting the fault may not have a vertical dip. In addition, the loci of maximum deformation either side of the surface rupture are offset by ∼20 km in a right-lateral sense. This is unusual—in most other cases of earthquakes studied using InSAR, the maxima of deformation do not show such an offset. It was this observation that led Peltzer *et al.* (1999) to propose an alternative, non-linear elastic rheology for the Manyi area; we will discuss the implications of this observation in later sections. Another notable feature of the interferograms is a second area where there is a clear symmetrical clustering, albeit smaller in extent, of fringes which are cut by an extension of the same decorrelated band. This feature, located in the centre of the western track (track 076), perhaps represents a second subevent of the earthquake.

The degree of correlation in all of the interferograms is high, with clear signal right up to the fault on both sides in many phases. This is most likely due to the short interval between the image acquisitions, the lack of agricultural activity and the low levels of vegetation at the high elevations of the Tibetan plateau. This high degree of data coverage, coupled with the low apparent levels of atmospheric noise, makes this an excellent data set for the purposes of understanding the faulting processes at work.

3 THE MANYI FAULT

An accurate knowledge of the surface location of the fault is a strong constraint on models of the earthquake source derived from geodetic data, reducing the number of unknown parameters, and preventing biases due to fault mislocation. To this end we first use a combination of data sets to study the geomorphology of the Manyi fault, the extent

Table 2. Descending track ERS–SAR data used in this study.

	Date 1	Sensor 1	Date 2	Sensor 2	$B_\perp$/m[a]	$\lvert h_a\rvert$/m[b]
Topographic data[c]						
Track 076	1996-May-04	ERS-1	1996-May-05	ERS-2	−102	98
Track 305	1996-April-13	ERS-1	1996-May-16	ERS-2	−104	96
Track 033	1996-May-01	ERS-1	1996-May-02	ERS-2	−101	99
Deformation data[d]						
Track 076	1997-March-16	ERS-2	1997-November-16	ERS-2	65	154
Track 305	1997-August-19	ERS-2	1997-December-02	ERS-2	4	2560
Track 033	1997-May-22	ERS-2	1997-December-18	ERS-2	−38	263

[a]Perpendicular baseline at image centre.
[b]Altitude of ambiguity at image centre.
[c]Topographic data are from frames 2889 and 2907 on the tracks mentioned.
[d]Deformation data are from frames 2871, 2889 and 2907 on the tracks mentioned.

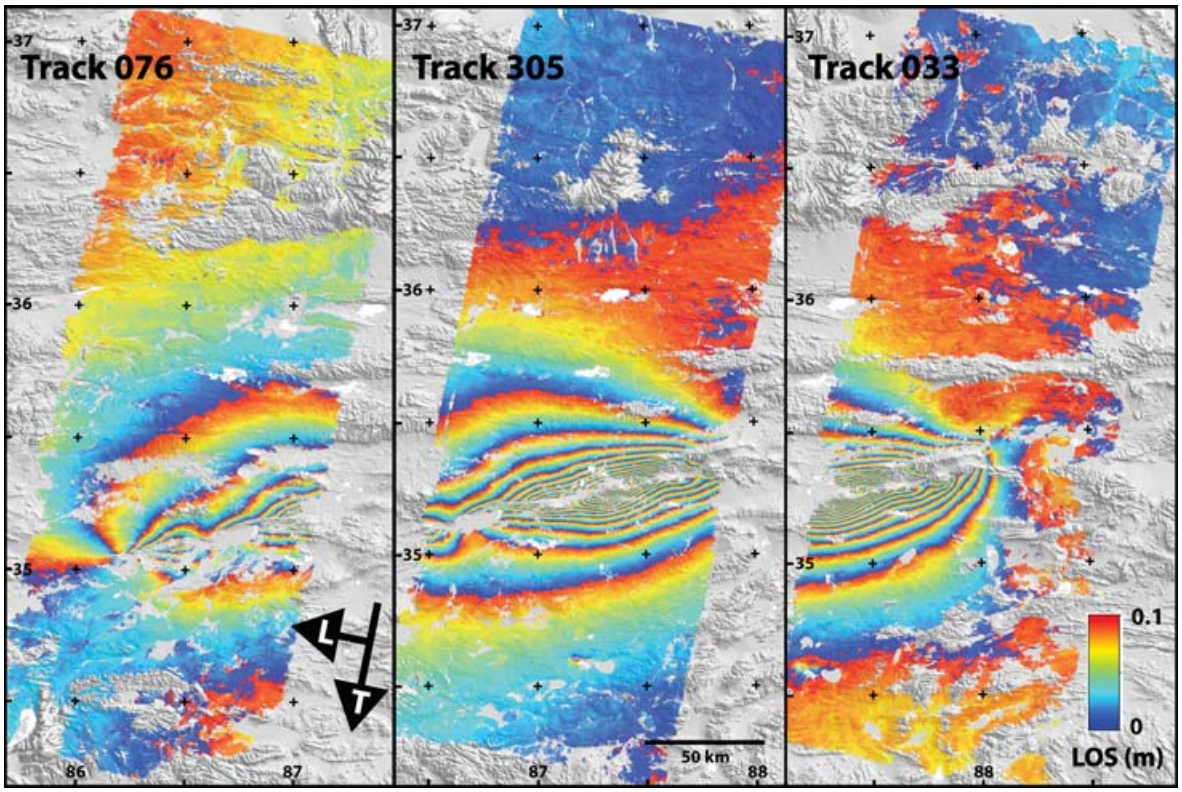

Figure 2. Manyi earthquake interferograms. Data shown are the unwrapped interferogram data, converted to line-of-sight (LOS) displacement of the ground and rewrapped at 0.1 m intervals. They are overlaid upon the Shuttle Radar Topography Mission digital elevation model used in the data processing, illuminated from an incidence angle of 45° from the northeast. The peak offset in LOS displacement is 2.4 m in both the central (305) and eastern (033) tracks, equivalent to a horizontal offset of ∼7 m if pure strike-slip deformation is assumed. The along-track (T) and LOS (L) directions are marked with arrows.

of the coseismic disturbance, and the coseismic fault offset in order to locate accurately its surface trace.

3.1 Geomorphic expression of the Manyi fault

The original identification of the Manyi fault was on the basis of its appearance in satellite photographs (Tapponnier & Molnar 1977). In the case of strike-slip faults like the Manyi fault, typical features include en echelon segmentation, offsets of geological markers, topographic features and drainage, vertical elevation changes due to local fault geometry (e.g. transpressive and/or transtensional features), and fault scarp formation (e.g. Yeats *et al.* 1997).

In order to investigate these phenomena, we use a combination of multispectral satellite imagery and high-resolution digital topography. The aftershock zone of the Manyi earthquake cuts across three LANDSAT-7 Enhanced Thematic Mapper tracks, from each of which we use two frames, all acquired after the event (Table 3). Images were selected, where possible, on the basis of minimal cloud and snow coverage, and assembled into a mosaic by manually adjusting the colour balances of adjacent scenes. The topographic data set that we use here is a high-resolution (40 m) DEM constructed from ERS tandem pair data (Table 2). Six frames from the three SAR swaths covering the epicentral region were processed using the ROI PAC software (Rosen *et al.* 2004). We prefer to use this data set for topographic analysis as it has higher resolution than the avalable SRTM DEM, and thus allows the discrimination of smaller-scale features. The tandem pair DEM was registered to the GTOPO30 elevation data set (http://edcdaac.usgs.gov:80/gtopo30/gtopo30.asp) to remove long-wavelength warps and tilts. Finally, we registered our LANDSAT mosaic to the DEM by manually selecting ground control points on prominent topographic features across the area of interest and computing a bicubic warp.

Table 3. LANDSAT-7 ETM data used to map the Manyi fault.

Path	Row	Date	Centre coordinates (Latitude, Longitude)
140	35	1999/08/25	36.042°N, 89.158°E
140	36	1999/08/25	34.608°N, 88.750°E
141	35	1999/09/17	36.042°N, 87.608°E
141	36	1999/09/17	34.608°N, 87.200°E
142	35	2001/07/11	36.042°N, 86.067°E
142	36	2001/07/11	34.608°N, 85.667°E

A perspective view of the high-resolution topography of the Manyi earthquake epicentral region, overlain by the false colour (RGB bands 541) LANDSAT-7 mosaic of the same area, is shown in Fig. 3. Along much of its length, the fault can be identified as a step or a cut in the landscape, or, in areas where there is little relief, as a sudden change in lithology (i.e. a change in colour) or a deflection in the orientation of a drainage channel across a linear boundary. In the sections that follow, we describe the key geomorphic features; distances quoted are measured along-strike from the westernmost point of the fault.

3.1.1 The western end of the fault (0–30 km)

At the western end of the aftershock zone, the surface trace of the Manyi fault is difficult to determine from the LANDSAT image alone (Fig. 4a). Evidence for three potential splays at this end of the fault can be identified in the high resolution topography (Fig. 4b);

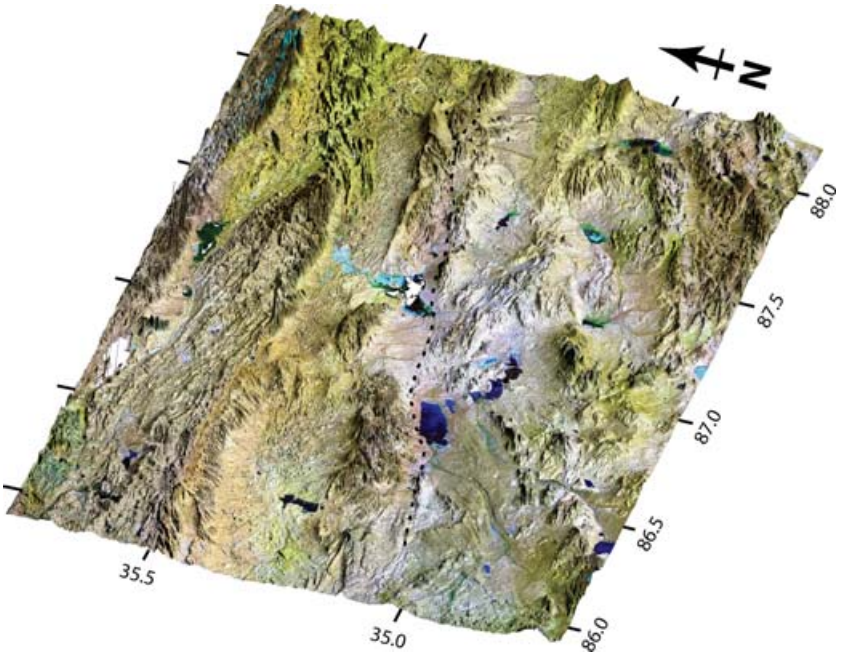

Figure 3. Perspective view of the Manyi fault from the WSW. The mapped fault trace is marked with a dashed line. Data shown are a subset of a LANDSAT-7 false colour mosaic (bands 541), overlaid upon a high resolution (40 m) digital elevation model constructed using ERS–SAR tandem pair images on three adjacent swaths (Section 3, Table 2).

corresponding features can then be identified in the LANDSAT image. Three linear ridges can be seen in the eastern half of Fig. 4(b), fanning out from east to west; in particular, the ridge in the north and that in the centre can be traced along-strike for at least 30 km in this area. Without the evidence from additional sources (such as the interfeometric decorrelation, see below) which suggest it was the central splay that failed in the 1997 earthquake, one might select the northern fault trace, the more contiguous structure; certainly it is possible that all three of the splays could be seismically active.

The central splay is defined in the topography by a discontinuous sequence of narrow (1–2 km wide) ridge segments, the longest of these extending for approximately 10 km. The surrounding terrain is flat and featureless, save for the putative fault splay features to the north and south, increasing the likelihood that these are pressure ridges, formed in response to a small local compressional component in the faulting. The exact location of the end of this splay, and therefore, the coseismic fault, in the west cannot be clearly identified from either the topography or the satellite imagery; we use the extent of the fault as estimated from interferometric decorrelation here.

3.1.2 Pull-apart basin (30–70 km)

The fault trace is at its most notable where it cuts across an alluvial fan system at 40–60 km along-strike. The fans build out southwards from a region of elevated topography north of the fault towards the north shore of an apparently shallow lake, the largest in the epicentral region, presumably occupying a pull-apart basin where the fault jogs to the left. The fault appears as a narrow white line, clearly offsetting the fan drainage channels in an enlargement of the LANDSAT image (Fig. 4c); the topography of the same area shows an abrupt break in the local slopes in the same location (central arrowhead, Fig. 4d). The LANDSAT image can be used to trace the same linear fault from the lake shore to both the west (where it again appears as a white line) and east (where it appears as a colour change in the image, presumably due to a lithological change across the fault). In the west of Fig. 4(d) it is difficult to locate the fault in the topography, except where there is again a break in slope on a embayment of the same elevated topography (location of the westernmost arrowhead in Fig. 4d); in the east of the same figure, the fault is marked by a narrow elongate push-up ridge as it is at its westernmost extent (Section 3.1.1 above), the ridge appearing to run immediately to the south of the fault.

3.1.3 Pressure ridge (90–130 km)

A second large lake, close to the mapped fault trace, is found between approximately 90 and 110 km along-strike. This lake appears to be ephemeral, with varying levels of water and snow in different satellite images. The fault can be identified as a change in lithology close to the southwestern tip of the lake (Fig. 4e). This feature can be traced eastwards in both the LANDSAT imagery and the digital topography (Fig. 4f) through a abrupt change in relief. To the north of the mapped trace lies a smooth, flat plain abutting the lake, to the south is a steeply sloping elevated ridge some 5 km wide, the trace having an approximately E–W trend at this location. Further east, the fault trace swings around to a more east–northeastward strike, visible in the LANDSAT imagery as a local colour change, presumably as a result of a localized lithology change, and in the topography by a very localized feature less than a kilometre wide. The development of the ridge can be explained as the effect of local transpression, where the fault undergoes a restraining right jog.

3.1.4 The cryptic eastern end of the fault (140–180 km)

As at its western end, in neither the elevation data nor the imagery is it clear where the fault trace goes at the eastern end of the aftershock zone. The fault trace can be mapped in the LANDSAT imagery (Fig. 4g), again as a colour change which probably represents a

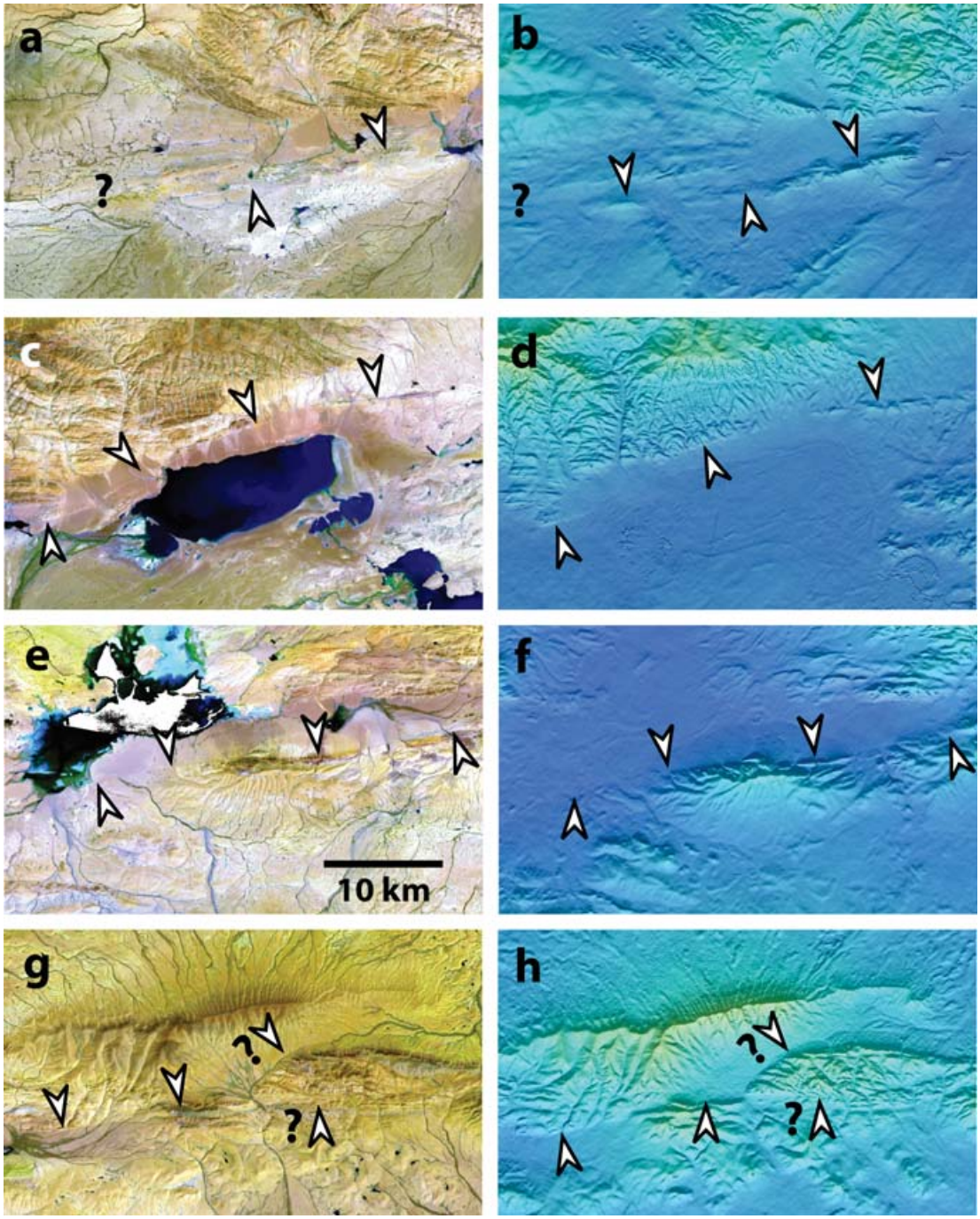

Figure 4. Mapping the Manyi fault. Identified fault features are indicated with white arrowheads. Each pair of images is comprised of a false colour (RGB bands 541) LANDSAT image (left) and a shaded relief DEM of the same area (right). (a and b) The western end of the Manyi fault. (c and d) The fault surface trace crossing a lake shore. (e and f) A double restraining bend in the fault, with pressure ridge. (g and h) The eastern end of the fault. (LANDSAT and DEM data as for Fig. 3. Locations of each subfigure are given in Fig. 6 and described within the text of Section 3.1.)

fault-related lithology change, up to the end of an approximately E–W trending lozenge-shaped ridge, located at approximately 160 km along-strike. Beyond here two branching splays can be identified (marked in Fig. 4g with question marks) flanking the ridge on either side, on the basis of a change in topography. The digital elevation data (Fig. 4h), where a single feature can be traced up to a ridge, before apparently dividing, suggests the same interpretation. Multiple candidates for the extensions of these two branches can be identified further to the east; without further information from interferometric correlation or azimuth offsets (see below), it is not possible to identify which of these is the active strand, or indeed whether either is active at all.

3.2 Mapping surface faulting with interferometric correlation

The interferometric correlation image is a by-product of InSAR processing. It provides a measure of the stability of the phase

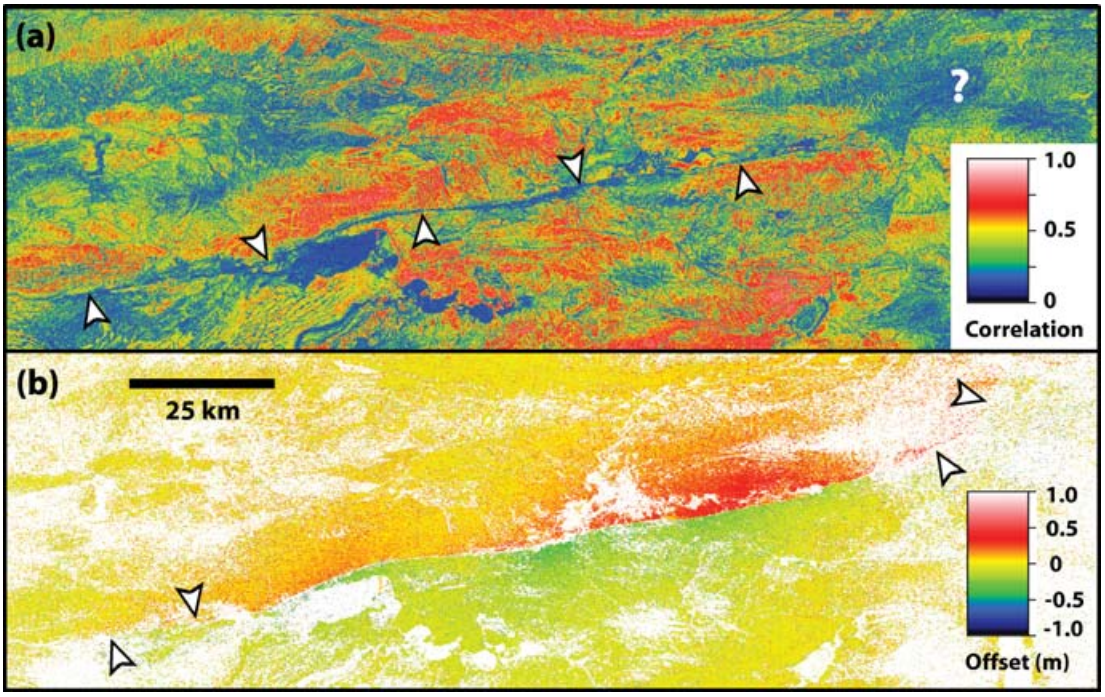

Figure 5. Mapping the Manyi fault using interferometric correlation and azimuth offsets. (a) Interferometric correlation. The fault can be traced as a dark blue band in the centre and the west, but not in the east. (b) Azimuth offsets. Here the fault can be traced as a discontinuity between positive and negative offsets all through the chosen area, even in the east. Further details are given in the text. Location of area shown defined in Fig. 6.

contribution of small radar scatterers within each interferogram pixel—if these scatterers are disturbed or modified in some way by some change to the surface, then the phase contribution of the pixel will change in a random fashion, and the correlation will be low; correlation will be high if the surface is unchanged. Typically objects or situations that can cause decorrelation of an interferogram pixel include the growth or movement of vegetation (in particular boreal forests); bodies of water; the falling or melting of snow; human activity (e.g. agriculture); high fringe gradients due to steep slopes, long perpendicular baselines between image acquisition points and/or large gradients in deformation at the surface; and physical disruption to subpixel scatterers due to natural hazards, such as floods, landslides or earthquakes. The probability of decorrelation also increases with the length of the interval between SAR image acquisitions.

In the case of a remote, barren area such as the Manyi region, many of these effects can be neglected—there is no human activity, and the extremely high elevations (modal elevation is ∼5 km) mean there no boreal vegetation. In practice it is also possible, through comparison using the elevation of each figure and its appearance using the LANDSAT and DEM data shown above (Section 3.1) to determine which decorrelation features are due to factors such as slope steepness or the presence of groundwater or snow at the surface. The remainder, in the case of the coseismic pairs of ERS-2 images for Manyi, can be interpreted as decorrelation caused by the surface rupture of the earthquake in that area.

A composite interferometric correlation image constructed from the coseismic pairs from all three ERS–SAR tracks is shown in Fig. 5(a). A prominent linear feature where the correlation is low can be seen along the length of the aftershock zone, most likely representing damage to the ground and steep displacement gradients created by the rupturing of the surface by the earthquake, as seen in other events (e.g. Simons *et al.* 2002; Talebian *et al.* 2004; Fielding *et al.* 2005). The linear decorrelation band extends further to the west than the fault traces mapped above, indicated by the westernmost arrowhead in Fig. 5(a). The location of the fault at the eastern end of the aftershock zone remains difficult to determine. A large decorrelated area close to the continuation of the fault in this area prevents the extension of the fault trace map here, but there is no convincing evidence in the decorrelation image for the fault adopting an E–W trend in this area.

3.3 Mapping the fault trace using azimuth offsets

Another means through which SAR data can be used to locate the active fault trace is through the calculation of azimuth offsets, the positional shifts required to precisely align the two SAR amplitude images in the along-track direction (Michel *et al.* 1999; Peltzer *et al.* 1999). In this way information about purely horizontal coseismic displacements in the along-track direction of the satellite is obtained, and any coherent discontinuity indicates the location of the fault. In the case of Manyi, the coseismic pairs of SAR images used to construct the interferograms were matched at four pixel intervals using the ROI_PAC program *ampcor*. To reduce the effects of noise and false matches in the data, offsets greater than 1 pixel in magnitude, equivalent to a movement of ∼4 m on the ground resolved into the along-track direction, were masked out, and a median filter was applied. Signal-to-noise ratios were further boosted by averaging of pixels in the along-track direction, and a planar trend, fitted to the data in the far-field away from the fault, was used to correct the data for long-wavelength signals due to the different observation positions of the satellite when the SAR images were acquired.

A composite image of the azimuth offsets for the three tracks is shown in Fig. 5(b). Although the fault orientation is almost perpendicular to the track direction of the satellite, a peak along-track offset of ∼1 m can be observed in the image at the location of

the InSAR decorrelation band. The level of false matches in the azimuth offset images is higher in the far field than the degree of incoherence in the interferograms, resulting in more patchy coverage, especially for the eastern track (track 033). However, azimuth offsets depend on the amplitude of the backscattered radar, a quantity that is less sensitive to surface change (and therefore decorrelation, see Section 3.2 above) than the interfeometric phase. In several areas therefore, the near-fault coverage is more comprehensive than that in the interferograms, especially around the eastern half of the fault.

As a result of this high level of near-fault coverage, the azimuth offsets offer the most comprehensive picture of the fault rupture of the various data sets used. The fault can be seen as a step in the offsets in Fig. 5(b), from red (positive along-track offset) to green (negative along-track offset). The fault can be traced along the length of the image, even in the east, where a step in the diffuse azimuth offset data (location indicated with arrowheads in Fig. 5b) enables us to see that the fault has swung towards a NE–SW trend in this area. Even though fault slip at this end of the fault is likely to be smaller than at the centre of the fault, this change in orientation towards the satellite descending track direction allows it to be identified.

3.4 The fault trace

Tracings of the Manyi fault from each of the different observations (Figs 4 and 5), are plotted together in Fig. 6. There is generally excellent agreement between the four traces along much of the length of the fault, especially in the central portion between 86.5°E and 87.5°E. At the western end of the fault (west of 86.5°E), there is agreement between the two traces derived from the SAR data – the azimuth offsets and interferometric correlation – but only poor constraints from the topography and LANDSAT imagery. At the eastern end (east of 87.5°E), the only continuous mapping comes from the azimuth offsets – as mentioned above, there is no convincing through going feature identified in any of the other data sets. Excepting this 'dog-leg' at the eastern end, the average strike of the main portion of the fault is approximately 258°, and shows broad agreement with the trend of the aftershock pattern located relative to the main shock by joint hypocentre determination (Robinson, private communication, 2005; Dewey 1971).

In order to simplify the overall, complex surface pattern of the fault, we fit the trace with a series of 11 straight line segments (Fig. 6). These are used as the basis of our uniform and variable-slip models, as developed below (Section 4). For the purposes of description, the fault segments are numbered from 1 to 11, starting with the westernmost segment.

4 OBTAINING SOURCE PARAMETERS USING ELASTIC DISLOCATION MODELLING

4.1 Data reduction

In order to expedite the modelling process, we utilize the high degree of spatial correlation in the interferogram to create a more manageable data set through downsampling. To achieve this we employ a modified quad tree decomposition algorithm (e.g. Jónsson *et al.* 2002), focusing the sampling, in this instance, on areas of high curvature in the line-of-sight displacements (e.g. Simons *et al.* 2002). A maximum block size of 10 240 m was selected based upon the e-folding lengthscale of the correlated noise in the interferograms (e.g. Wright *et al.* 2003; Wright *et al.*, in preparation). For each interferogram, this reduced the number of data points from several million to ∼1500–2000. We choose not to use the azimuth offset data in the inversion process for two reasons. As the offsets are measurements in the satellite along-track direction, they are relatively insensitive to motion parallel to the Manyi fault; in addition, the offsets have a noise level one to two orders of magnitude larger than the InSAR data and would, therefore, have a very low weighting in, and influence on, the inversion for the additional computation required.

4.2 Single fault uniform slip models

For a first-order description of the Manyi earthquake source, we model the resampled displacements using a single rectangular elastic dislocation in a uniform half-space (Okada 1985). We solve for nine parameters describing this dislocation – its strike, dip, rake, slip, latitude, longitude, length, top and bottom depths – using a downhill simplex algorithm with multiple Monte Carlo restarts (e.g. Clarke *et al.* 1997; Wright *et al.* 1999) to obtain the set of parameters

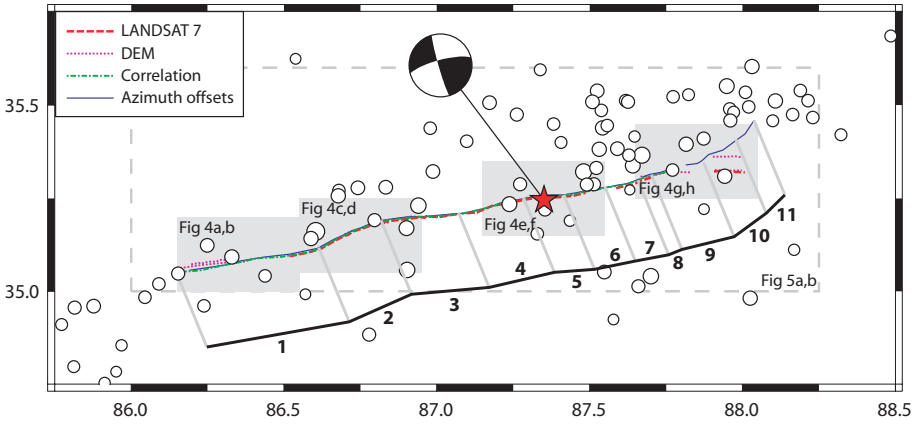

Figure 6. The mapped Manyi fault trace. Four mapped traces of the Manyi fault (red, blue, green and magenta lines), constructed by tracing features on each of four data sets, are compared. There is good agreement between the various measures, especially in the central portion of the fault. A simplified fault trace (black line), composed of eleven straight fault segments, used in subsequent modelling is also shown. Details of the length and location of the numbered fault segments are given in Table 4. Grey transparent boxes indicate the locations of the images in Fig. 4, grey dashed box gives location of images in Fig. 5. Relocated aftershock data (white circles), located relative to the hypocentre of Steck *et al.* (2001; red star) provided by Robinson (private communication, 2005). Main shock focal mechanism is taken from Velasco *et al.* (2000).

Table 4. Fault geometry and source parameters of uniform slip models.

		Latitude[a]	Longitude[a]	Strike	Dip[b]	Rake	Slip (m)	Length (km)	Top (km)	Bottom (km)	M_0 (N m)	rms (m)[c]
1 fault		35.258°	87.358°	259.5°	85.2°	−2.7°	5.76	83.9	0.0	10.1	1.68×10^{20}	n/a (0.092)
11 fault[d]	1	35.084°	86.380°	260.4°	86.5°	−11.2°	1.38	43.1	0.0	12.6		
(single dip)	2	35.155°	86.715°	246.2°	86.5°	−11.2°	1.58	20.3	0.0	12.6		
	3	35.201°	86.943°	264.9°	86.5°	−11.2°	2.74	23.3	0.0	12.6		
	4	35.231°	87.177°	256.9°	86.5°	−11.2°	4.34	19.9	0.0	12.6		
	5	35.255°	87.350°	265.5°	86.5°	−11.2°	5.34	12.0	0.0	12.6		
	6	35.270°	87.482°	258.2°	86.5°	−11.2°	4.68	12.5	0.0	12.6	2.18×10^{20}	0.079 (0.064)
	7	35.290°	87.604°	259.0°	86.5°	−11.2°	3.64	10.1	0.0	12.6		
	8	35.306°	87.680°	247.1°	86.5°	−11.2°	3.31	4.3	0.0	12.6		
	9	35.329°	87.787°	256.1°	86.5°	−11.2°	2.89	16.0	0.0	12.6		
	10	35.378°	87.925°	233.1°	86.5°	−11.2°	2.12	11.8	0.0	12.6		
	11	35.447°	88.023°	224.6°	86.5°	−11.2°	0.00	11.7	0.0	12.6		
11 fault[d]	1	35.084°	86.380°	80.4°	85.5°	2.6°	2.04	43.1	0.0	11.7		
(reversing dip)	2	35.155°	86.715°	66.2°	85.5°	2.6°	2.74	20.3	0.0	11.7		
	3	35.201°	86.943°	84.9°	85.5°	2.6°	4.32	23.3	0.0	11.7		
	4	35.231°	87.177°	76.9°	85.5°	2.6°	6.73	19.9	0.0	11.7		
	5	35.255°	87.350°	265.5°	84.3°	−9.3°	5.34	12.0	0.0	14.2		
	6	35.270°	87.482°	258.2°	84.3°	−9.3°	4.91	12.5	0.0	14.2	2.63×10^{20}	0.066 (0.052)
	7	35.290°	87.604°	259.0°	84.3°	−9.3°	3.67	10.1	0.0	14.2		
	8	35.306°	87.680°	247.1°	84.3°	−9.3°	3.16	4.3	0.0	14.2		
	9	35.329°	87.787°	256.1°	84.3°	−9.3°	3.07	16.0	0.0	14.2		
	10	35.378°	87.925°	233.1°	84.3°	−9.3°	0.18	11.8	0.0	14.2		
	11	35.447°	88.023°	224.6°	84.3°	−9.3°	0.00	11.7	0.0	14.2		

[a]Location of the centre of the fault plane projected up-dip to the surface.
[b]A right-hand convention is assumed for dip direction (i.e. faults with a westward strike-dip to the north and eastward-striking faults dip to the south).
[c]Root-mean-squared misfit to data points located at distances >750 m from the fault surface trace (values in parentheses: misfit to data points >3 km from the trace).
[d]Fault segments are numbered from west to east.

corresponding to a global minimum misfit between the model and the data. In addition, we solve for three nuisance parameters for each displacement data set – a static shift in measured displacement, and gradients of displacement in the east-west and north–south directions – to account for zero-level ambiguities and any residual long wavelength orbital errors, respectively. As the mapped fault trace is complex, and inverse models of this type can be appreciably biased when trying to fit data from the 'wrong' side of the fault, data points located within 3 km of the mapped fault trace were excluded from this inversion.

The model we obtain (Table 4; Fig. 7), shows 5.76 m of near-pure left-lateral strike-slip displacement on a 84 km-long fault, striking parallel to the aftershock trend, and dipping steeply northward. Although the level of fit is acceptable in the furthest far-field (at distances ≥100 km from the fault trace), elsewhere the model shows a poor fit to the data, as evidenced by its large root mean squared (rms) misfit value for the restricted data set used in the modelling (0.092 m) and the large numbers of residual fringes that remain when the synthetic model is subtracted from the real data (Fig. 7g). Misfits are commonly of the order of 0.5 m or greater in amplitude in areas near the mapped fault trace. The fit is especially poor in the western half of the fault, where the residual displacements are not only large in amplitude near the fault trace, but significant over large distances away from it, with over 0.1 m of residual displacement at distances of ∼40 km. The poor fit in the west is most likely due to the presence in this area of the second cluster of fringes, possibly due to a second subevent of the earthquake (see Section 2.1 above), that a single elastic dislocation cannot fit. In addition, the presence of 'alternating' clusters of residual fringes either side of the mapped fault in the central track, which are located on the insides of bends in the mapped fault trace, suggest that there is first-order structure to the deformation pattern that cannot be explained by a single straight fault. The relatively low seismic moment for this model, when compared with those obtained seismically (Table 1) is additional evidence that such a simple model cannot satisfactorily describe the Manyi earthquake.

4.3 Multiple fault uniform slip models

Seismological studies of the Manyi earthquake suggest that it was a complex event with multiple subevents (Velasco *et al.* 2000). In addition, we have already demonstrated that the surface trace of the coseismic fault deviates significantly from a straight line, and may be segmented. Therefore, a reasonable step that can be taken to improve the level of fit to the data is to use a fault with multiple segments, estimating the amount of slip on each separately. We adopt the simplified 11 segment fault geometry already described above (Section 3.4), fixing the surface location, strike and length of each fault segment. Given that the effects of a fault rupture can be observed in the interferometric correlation along the length of the fault, it is reasonable to also fix the top depth of all of the faults to be zero. The remaining four fault parameters for each segment (dip, rake, bottom depth and slip) can then be determined using the same downhill simplex/Monte Carlo method as above. It is not possible to solve efficiently for every parameter on every segment simultaneously—such an undertaking would be extremely expensive computationally, and subject to problems of trade-off and non-uniqueness. Therefore, we simplify the inverse problem by solving for a single value of dip, rake and bottom depth for multiple fault segments, whilst simultaneously solving for the slip on each segment. We model two scenarios, as described below. In both cases, data points less than 750 m from the fault trace were excluded, the distance being sufficient for no data points to fall on the 'wrong' side of the simplified fault trace.

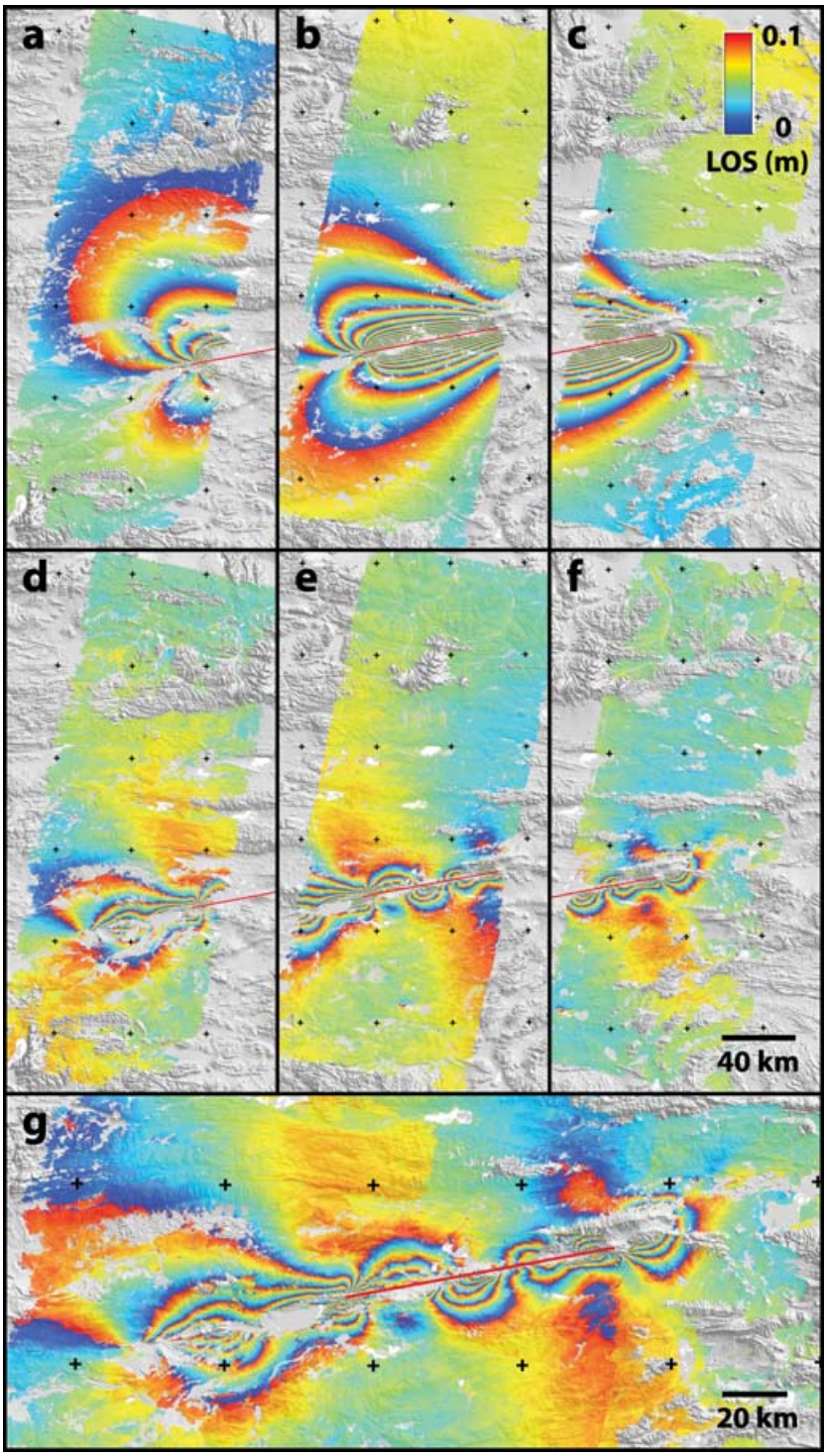

Figure 7. Single dislocation model of the Manyi earthquake. (a–c) Model interferograms for tracks 076, 305 and 033, respectively. (d–f) Residual interferograms (data−model) for tracks 076, 305 and 033, respectively. Locations of (a–f) as for the observed interferograms in Fig. 2. (g) Near-fault detail of a composite of all three residual interferograms. Details of the model given in Table 4. Further description and interpretation given in the main text.

4.3.1 A single-dip fault model

The simplest case we consider is that where all of the 11 fault segments are constrained to have the same dip, rake and bottom depth. Our best-fitting model of this type is listed in Table 4, with synthetic and residual interferograms plotted in Fig. 8. As in the case of the single fault model, the fault dips steeply to the north; the rake is again close to pure left-lateral strike-slip, with a slightly larger normal component in this case. There is a peak of 5.34 m of slip at the centre of the fault, somewhat less than the 7 m offset that can be inferred directly from the interferogram, suggesting that there may be a concentration of slip at shallow depths which cannot be resolved by this model. No slip is required on the easternmost (and most poorly constrained) fault segment. The model seismic

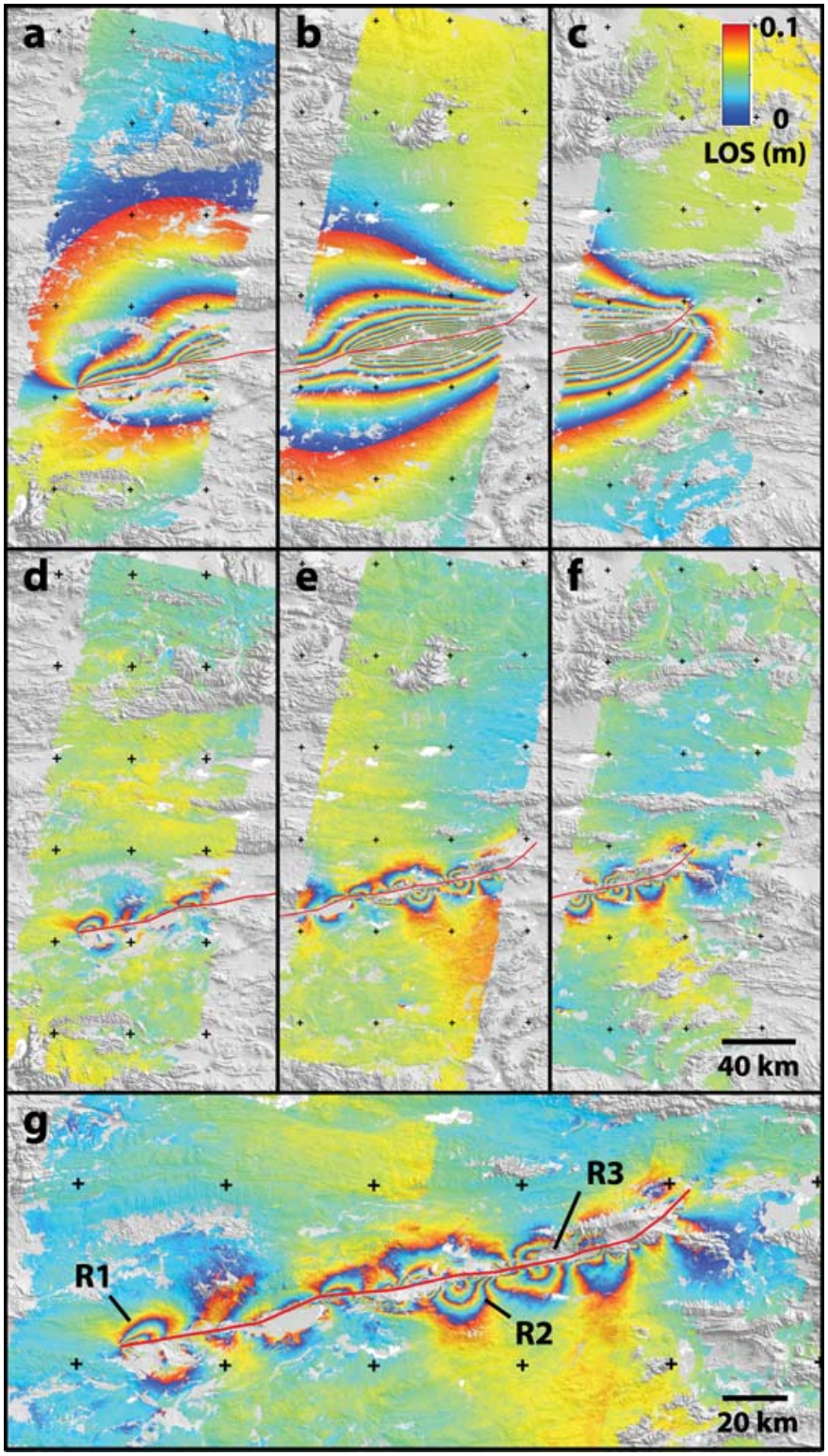

Figure 8. Multiple segment uniform slip model of the Manyi earthquake, with a single dip, rake and bottom depth. Elements (a–g) as for Fig. 7. R1–R3 are residual features described in the main text. Details of the model given in Table 4.

moment, 2.18×10^{20} N m, is consistent with values obtained by seismological studies (Table 1).

As might be expected, this model shows a substantial data-fitting improvement over the single fault case, with significantly lower rms misfits, where the misfit to the same reduced data set is calculated (Table 4), and dramatically fewer residual fringes over distances of 5–40 km from the fault (Fig. 8g). The fit is especially good between segments 2 and 4 in the west, and segments 8 and 11 in the east, where residuals are small and local to the fault trace. Significant residuals (∼0.3 m) still remain at both the westernmost end of the

fault (labelled R1 in Fig. 8g), possibly reflecting the uncertainty in the extent of the fault in this area. There are also notable residuals in the centre of the fault (corresponding to fault segments 4–7). The most interesting of these residual features is a cluster of residual fringes on the south side of the fault in the bend between fault segments 4 and 5 (labelled R2 in Fig. 8g). These fringes appear to represent one half of the asymmetric deformation feature in the interferogram noted by Peltzer *et al.* (1999). It is clear that a fault model with a single, steep dip cannot fit the fringes on both sides of the fault in this location. The final large residual (labelled R3 in Fig. 8g) is a symmetrical feature that probably reflects a variability in the amount of slip with depth that cannot be resolved by a uniform slip model.

4.3.2 A reversing-dip fault model

The second scenario we model is the case where the fault has a change in its dip, rake and bottom depth somewhere along its length. The fault segments are divided into two groups and a single dip, rake and bottom depth solved for each, doubling the number of geometric parameters to be solved by the hybrid simplex/Monte Carlo algorithm over the previous scenario. A number of different groupings are tried. The best-fitting of these models is listed in Table 4 and displayed in Fig. 9. In this model, the first group, comprised of segments 1–4, dips steeply to the south, and the remaining segments dip steeply to the north as before. This reversal in dip is accompanied by an increase in bottom depth moving from west to east, and a small change in rake, although given the change in dip direction, the sense of vertical motion on each side of the fault remains the same. The peak in slip is located in the vicinity of the dip reversal on the fourth fault segment, and at 6.73 m is close to that inferred from the fringe offset at the fault. Again there is no slip required on the easternmost fault segment. The total seismic moment of 2.63×10^{20} N m is higher than the seismic estimates listed in Table 1, but not substantially so.

The reversing-dip model shows an improvement in the rms misfit to the data of around 20 per cent over the single dip scenario. Qualitatively, it seems that the level of misfit, represented by the distribution of residual fringes, is improved in general along the fault, with the possible exception of the very eastern end. The most striking improvement in the residual fringe pattern is in the central portion of the fault (segments 4–7). Here, the feature associated with the interferogram asymmetry present in the residual interferogram for the single dip case (labelled R2 in Fig. 8g), has been dramatically reduced in amplitude, suggesting that the asymmetric pattern seen in the original interferogram may be due to a change in fault geometry at this location. Some significant residuals remain—again, at the western end of the fault, and in the vicinity of the seventh fault segment (the feature labelled R3 in Fig. 8g). In general, however, we are satisfied that the reversing-dip model provides a more satisfactory description of the deformation pattern, and use it as the basis of the more detailed modelling below.

4.4 Multiple fault variable slip models

The tests with uniform-slip models demonstrate that it is not possible to reproduce all of the deformation observations satisfactorily using such models. One explanation for this may be that the set of fixed fault segments does not accurately describe the geometry of slipping areas on the fault, so that some portions of fault segments have inappropriate levels of slip forced upon them. This problem is exacerbated by the excellent data coverage close to the fault along the majority of its length from the high coherence in the interferograms, which is likely to have greater resolving power than uniform slip models can satisfy. Therefore, it is likely that if the slip on each fault segment is allowed to vary spatially, there will be significant improvements to the fit to the data compared to the equivalent uniform slip case.

4.4.1 The fixed rake case

For a first variable slip model, we use the geometry of the best-fitting uniform slip model obtained above, extending the model fault to a depth of 20 km and divided into patches approximately 4×4 km in dimensions—giving a total of 47 divisions along-strike and five divisions downdip. (Full details of the fault parametrization and its location in space, and of modelled fault slip are given in an online supplement: URL.) We fix values of rake for each fault segment to those obtained in the uniform slip inversion. The value of the slip on each fault patch is linearly related to the displacements measured using InSAR, and can thus be obtained using a least-squares inversion process. We also solve linearly for nuisance parameters relating to the zero-level ambiguity in slip and residual orbital tilts in the N–S and E–W directions for each data set, as for the uniform slip case. We impose a Laplacian smoothing criterion to prevent unphysical oscillatory slip, and solve the least-squares problem using the Fast Non-Negative Least-Squares (FNNLS) algorithm (Bro & De Jong 1997), thus explicitly removing the possibility of retrograde fault motion in the model. Further details of the model formulation and of resolution testing are given in Appendix A.

Our model results, along with synthetic and residual interferograms showing the fit to the data, are shown in Fig. 10, with details listed in Table 5. Slip is concentrated within the upper 8 km of the fault, peaking at 7.46 m at a distance of 100 km along-strike. Up to four areas of high slip, or asperities can be identified within the slip pattern. Three – those between 76 and 92 km, 96 and 116 km, 124 and 132 km along-strike – form a connected chain, comprising the area of maximum moment release, with a fourth located between 152 and 160 km along-strike. All significant slip is concentrated within the upper 8 km of the fault, which is also the region of peak model resolution (Appendix A3, Fig. A2). In keeping with the observed second cluster of interferogram fringes in the west (Fig. 2), there is also a small peak in slip at the western end of the fault (between 20 and 32 km along-strike). Everywhere on the fault, the 1σ uncertainties, estimated by a Monte Carlo process (Section A2), are less than 10 cm, indicating that the slip pattern is well constrained. The total seismic moment, of 2.52×10^{20} N m, is around 10 per cent higher than the available seismic estimates (Table 1), but is smaller than that obtained in the uniform slip case above (Section 4.3.2), suggesting that slip has been removed from areas that did not require it in the previous case.

As might be anticipated, the degree of fit is improved over the uniform slip case, with residuals that are smaller in amplitude, and located closer to the fault, reflected in the reduced rms misfit of 0.052 m. One prominent residual remains, however, to the south of fault segment 7, between 132 and 144 km along-strike. The polarity of this residual feature suggests that slip may be underestimated in this area by the fixed rake model.

4.4.2 The variable rake case

A further refinement of the variable slip model described above can be made by allowing the rake to vary between fault patches. We

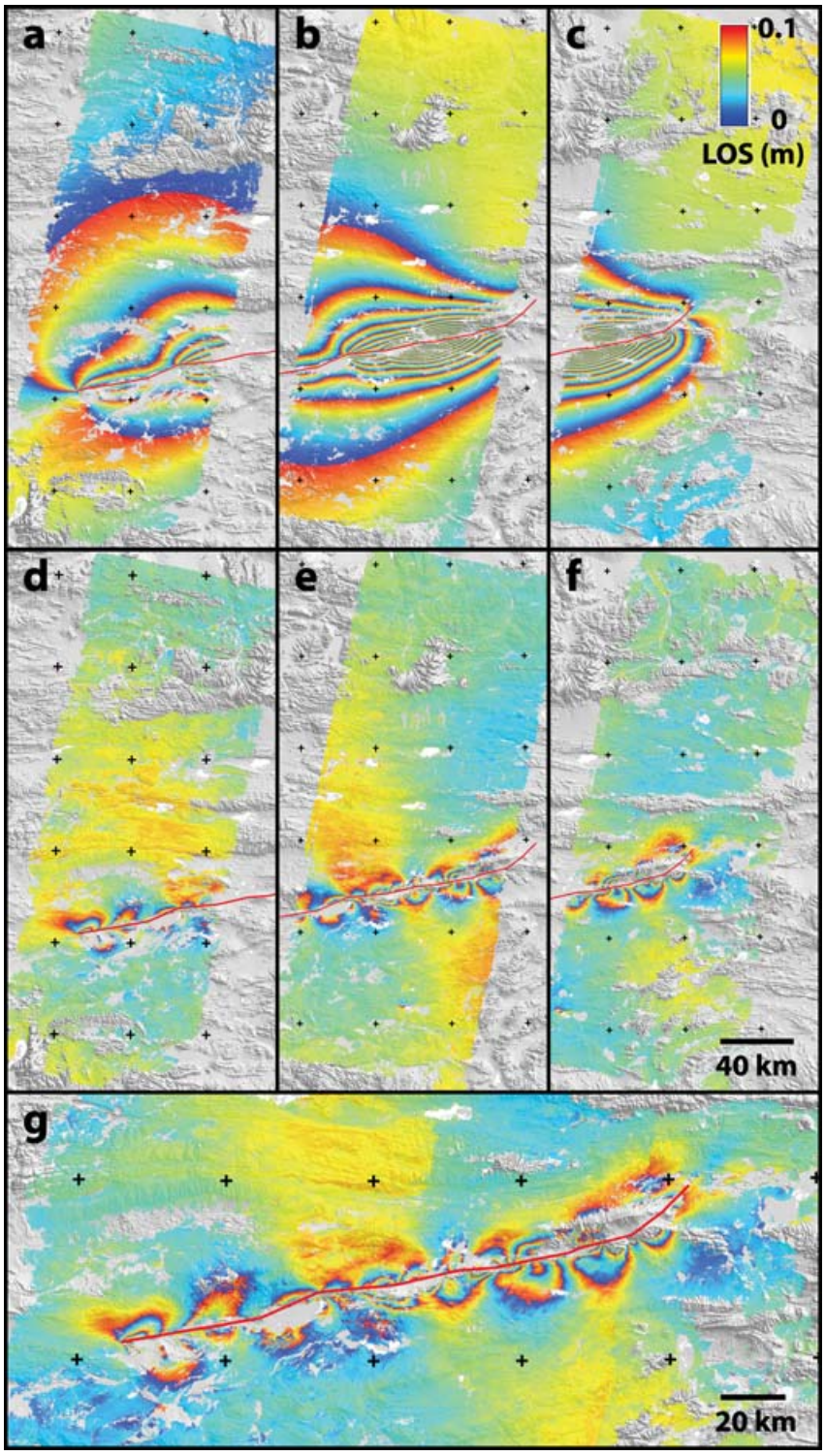

Figure 9. Multiple segment uniform slip model of the Manyi earthquake, with an along-strike change in dip, rake and bottom depth. Elements (a–g) as for Fig. 7. Details of the model given in Table 4. Further description and interpretation given in the main text.

achieve this by defining two basis functions for slip on each fault patch—one with a rake of −45° and the other with a rake of 45°. The best-fitting combination of slip in both of these basis directions in a least-squares sense can then be used to estimate both the slip and the rake for each fault patch. If the FNNLS algorithm is used to obtain the solution, as for the fixed rake case above, then the rake is effectively bounded between −45° and 45°. All other aspects of the inversion (e.g. smoothing and nuisance parameters) are conducted as for the fixed rake case. Further details of the formulation of the model and of its resolution are given in Appendix A.

Our model results, along with synthetic and residual interferograms showing the fit to the data, are shown in Fig. 11, with details listed in Table 5. The differences between this model and the fixed rake model are perhaps surprising. The region of greatest slip in

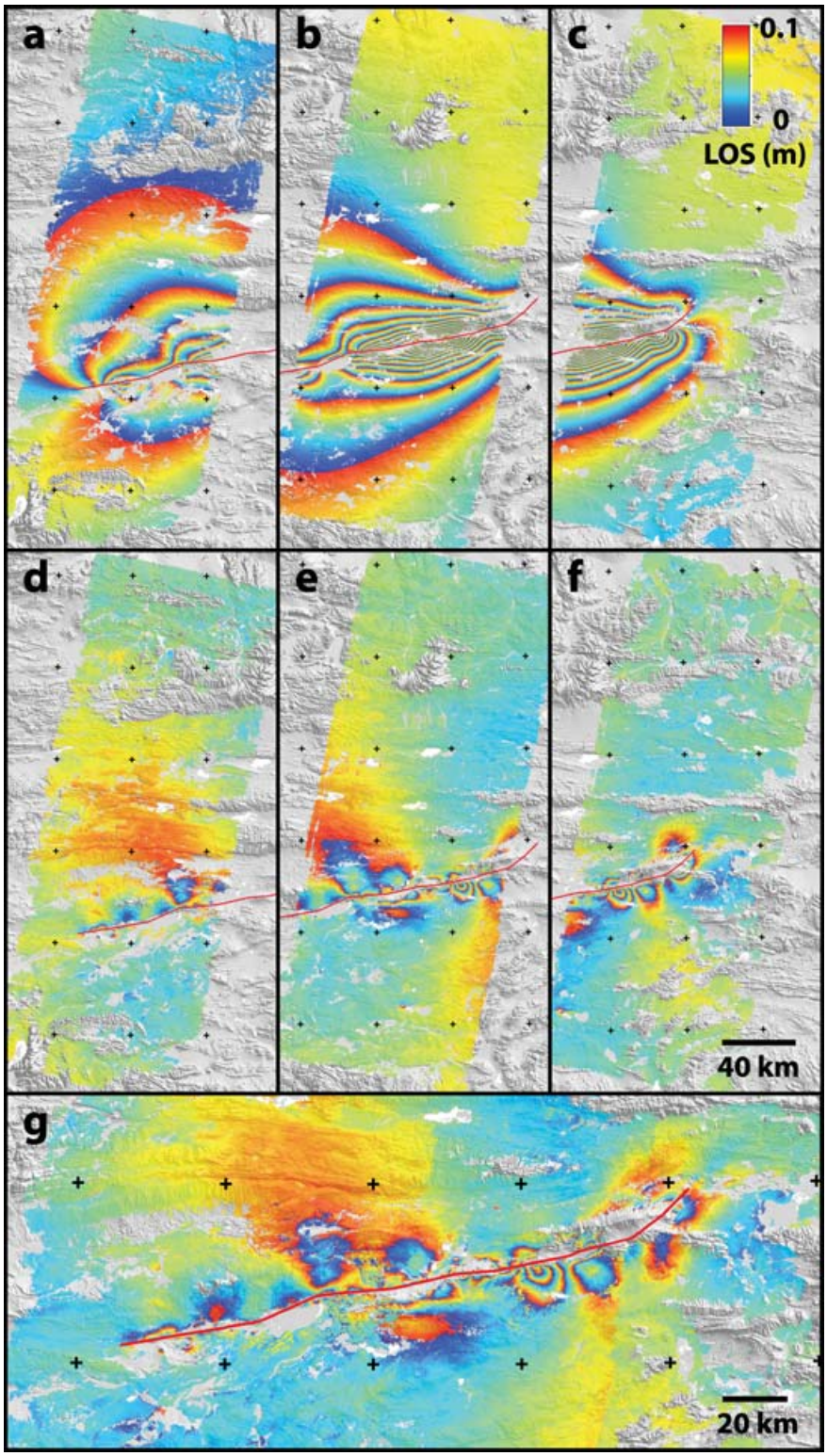

Figure 10. Fixed rake variable slip model of the Manyi earthquake. Elements (a–g) as for Fig. 7. (h) Magnitude and uncertainty (σ_{slip}) of fault slip. Arrows indicate direction of displacement of the south side of the fault with respect to a fixed north side. Further description and interpretation given in the main text.

the fixed rake model was long and narrow, composed of three connected asperities between 76 and 132 km along-strike, with a fourth asperity further to the east, all confined to the upper 8 km of the fault. In the variable rake model, there are only two large asperities, and in general slip occurs down to greater depths. In all areas, the scale of the modelled fault slip features in the upper 12 km of the crust is equal to or less than the minimum resolvable distance in those areas; slip features on the lower 8 km of the fault are poorly

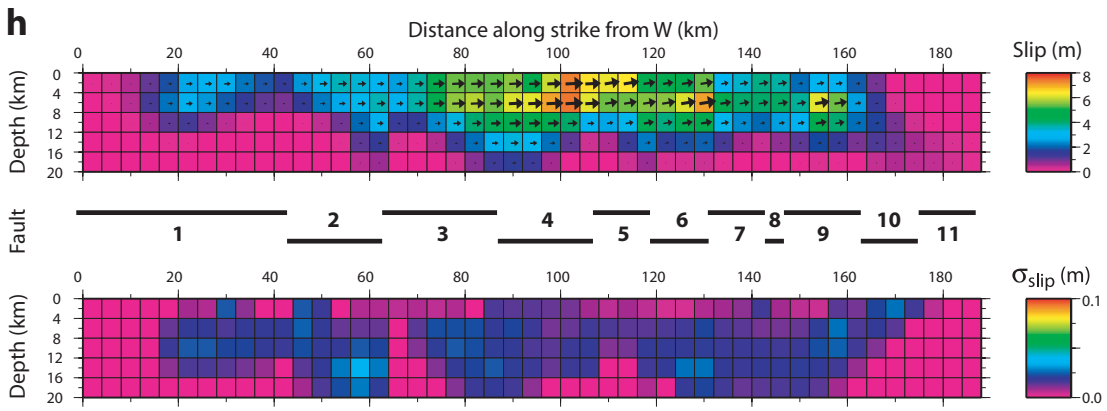

Figure 10. (*Continued.*)

Table 5. Parameters of variable slip models.

	κ	$M_0/10^{20}$ (N m)	rms misfit (m)
Fixed rake	850	2.52	0.052 (0.040)[a]
Variable rake	700	2.84	0.028 (0.021)[a]

[a]Values in parentheses represent the misfit for the same model where data less than 3 km from the fault trace are excluded.

resolved (Section A3, Fig. A2). The larger of the two aperities is located in the region of the double restraining bend (Section 3.1.3) between 100 and 124 km along-strike, and has a peak of ∼7 m of slip, with ∼5 m of slip occurring down to 16 km depth. The second asperity, with peak slip of 7.64 m, is located between 128 and 144 km along-strike, corresponding to the area of the largest residuals in the fixed rake model (Fig. 10g), which have been almost totally suppressed in this case (Fig. 11g); this asperity has no analogue in the fixed rake model.

Another key difference between the two models is the generally lower magnitude of surface slip shown by the variable rake model. With the exception of the second asperity, surface slip in the variable rake model is around 5 m or less, compared with 6 m or greater in the fixed rake model. As the 1σ uncertainties in slip are everywhere less than 20 cm, and 10 cm or less in the upper layer of fault patches, these differences are significant. The high fringe rates seen in the near fault areas in the variable rake model must, therefore, be due to the larger modelled components of dip-slip motion seen in the near surface layer of fault patches. Variations in these dip-slip motions, manifest as changes in rake of 20° or greater that are significantly greater than the 5° uncertainties corresponding to those fault patches, are particularly large in the area of the double restraining bend (fault segments 4–6, 100–124 km along-strike). This suggests that the local fault geometry exerts a strong control on the pattern of fault slip in this area.

In general, the fit to the data of the variable rake model is excellent given the high level of coherence, and therefore, data coverage on both sides of the fault. There are few residual fringes in the near field, particularly in the western and central tracks, and no significant residuals in the far field, reflected in the rms misfit of 0.028 m—almost a factor of 2 improvement in fit. The total geodetic moment, of 2.84×10^{20} N m, is again larger than the moment estimates from seismic data (Table 1). This could be due to the presence of a small degree of early post-seismic motion in the coseismic interferogram (see Section 5.3 below).

5 DISCUSSION AND CONCLUSIONS

5.1 Subevents of the Manyi earthquake

Our studies of the geomorphology of the Manyi fault zone, and the surface displacements of the 1997 earthquake have revealed the Manyi fault to be a complex geometrical structure, with considerable heterogeneity in slip along its surface. Our preferred model for the 1997 earthquake (Section 4.4.2, Fig. 11), in which both the amount and direction of slip are allowed to vary on a fault geometry consistent with the mapped surface trace, and which contains a reversal in the fault dip located in its central portion, indicates that the majority of moment release occurred within the upper 12 km of the fault and within a 44-km-long zone along-strike.

The identification of a relatively narrow zone in which the largest fault slip occurrs may provide limited support for the body wave inversion model of Velasco *et al.* (2000), who identify five subevents for the Manyi earthquake, all occurring within 25 km of the hypocentre. As the hypocentre in this case is located within fault segment 5 (Steck *et al.* 2001, Fig. 6), it is possible that the zone of peak moment release could represent the superposition of the slip due to several, or indeed all, of these subevents; however, the location of the second cluster of fringes at distances of ∼80–90 km to the west of the hypocentre (Fig. 2), suggest that at least one subevent should be located substantially further to the west. Preliminary attempts to reconcile teleseismic body wave data with the InSAR displacements by jointly inverting the two data sets suggest that two peaks on the source time function for the earthquake later than 30 s after the rupture initiation represent slip subevents at distances greater than 60 km west of the hypocentre (Funning 2005; Fukahata *et al.* 2005; Funning *et al.*, in preparation), in keeping with the significant levels of slip seen in our model at such distances (Fig. 11h).

5.2 Mechanisms for generating interferogram asymmetry

A key feature that must be explained in elastic modelling of the Manyi interferograms is the asymmetry that can be seen in both the central and eastern track interferograms (Figs 2 and 12a). Peltzer *et al.* (1999) suggested that such a deformation pattern required the crust to have different elastic moduli in the dilatational and compressional quadrants of the earthquake, that is, different rigidities under compression and tension. However, in almost all other cases of earthquakes studied with InSAR, including the nearby 2001 Kokoxili

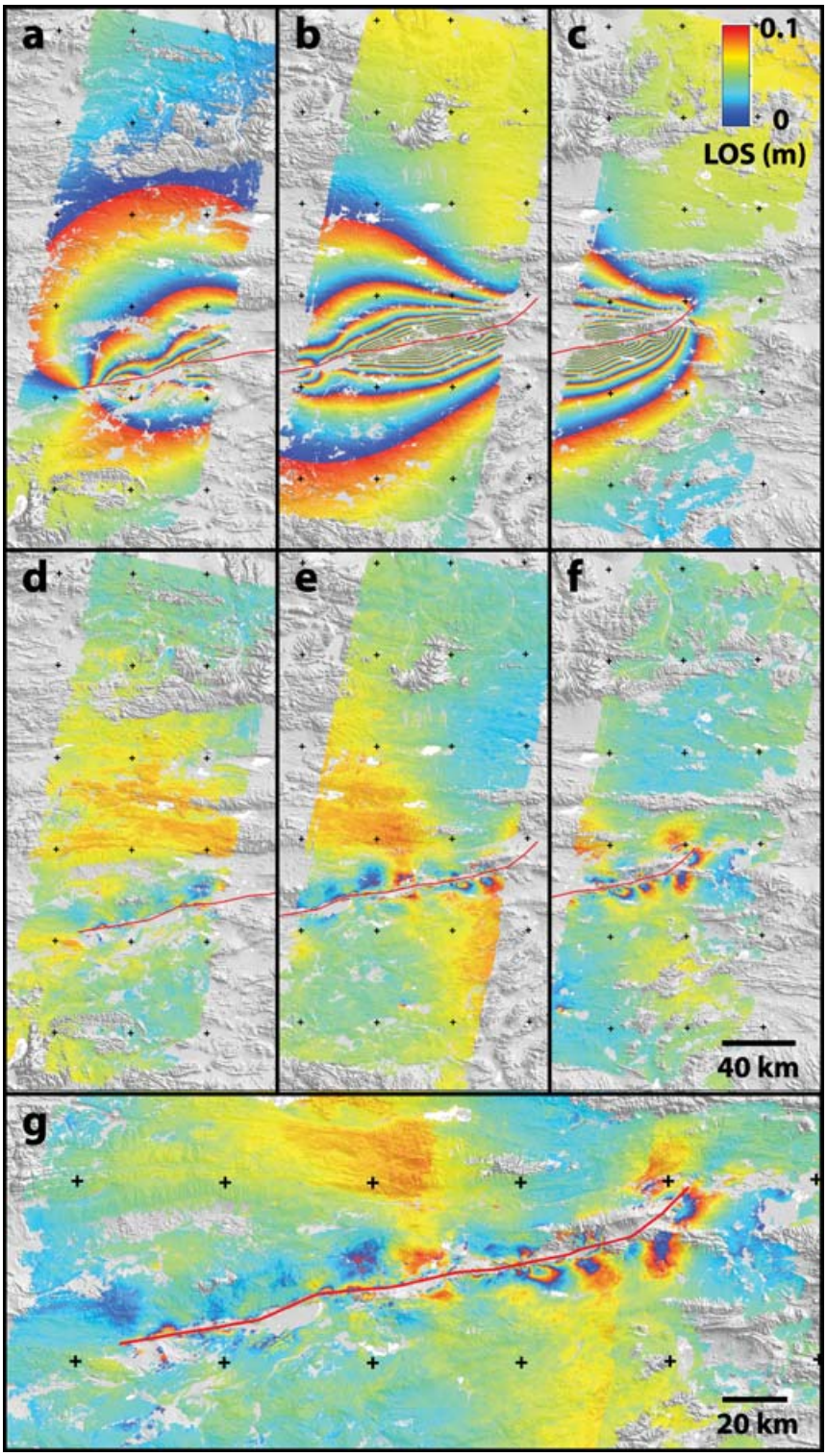

Figure 11. Variable rake and slip model of the Manyi earthquake. Elements (a–g) as for Fig. 7. (h) Magnitude and direction and associated uncertainties (σ_{slip} and σ_{rake}, respectively) of fault slip and rake. Arrows indicate direction of displacement of the south side of the fault with respect to a fixed north side. Further description and interpretation given in the main text.

event (Lasserre *et al.* 2005), such a rheology is not required, and as we have shown above, it is also possible to explain the observations for the Manyi earthquake without this requirement.

To understand the physical basis of the asymmetry in the fringe pattern, consider the geometry of faults shown in Fig. 12(b), which shows fault segments, corresponding to fault segments 4, 5 and 6, forming a minor right jog. In the simple model considered, all three faults have the same, pure left-lateral rake, the same slip (6 m) and the same minimum and maximum depths (0 and 10 km, respectively). The westernmost fault segment has a dip of 80° to the south,

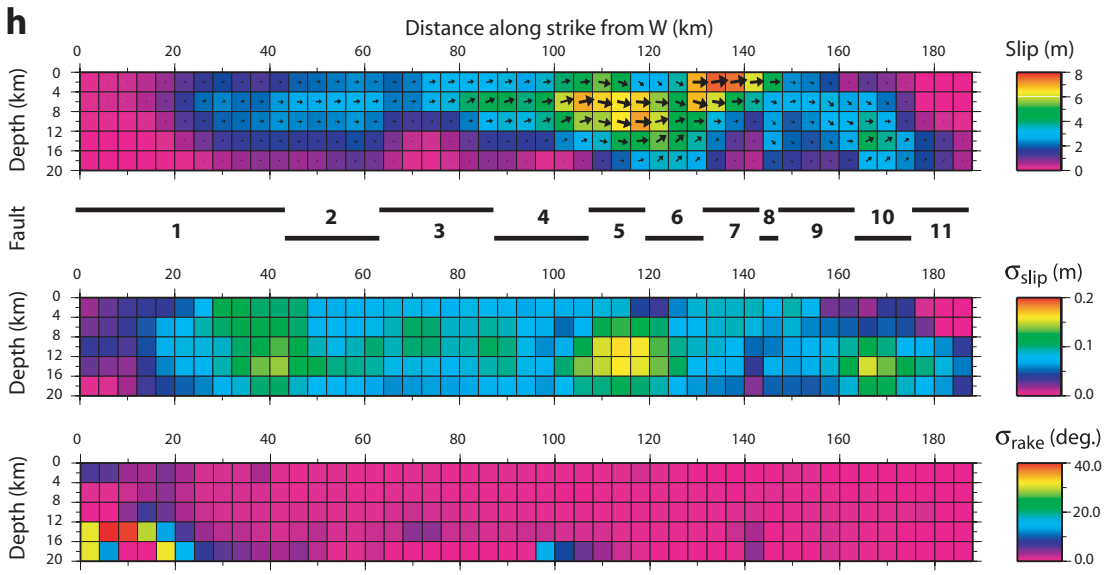

Figure 11. (*Continued.*)

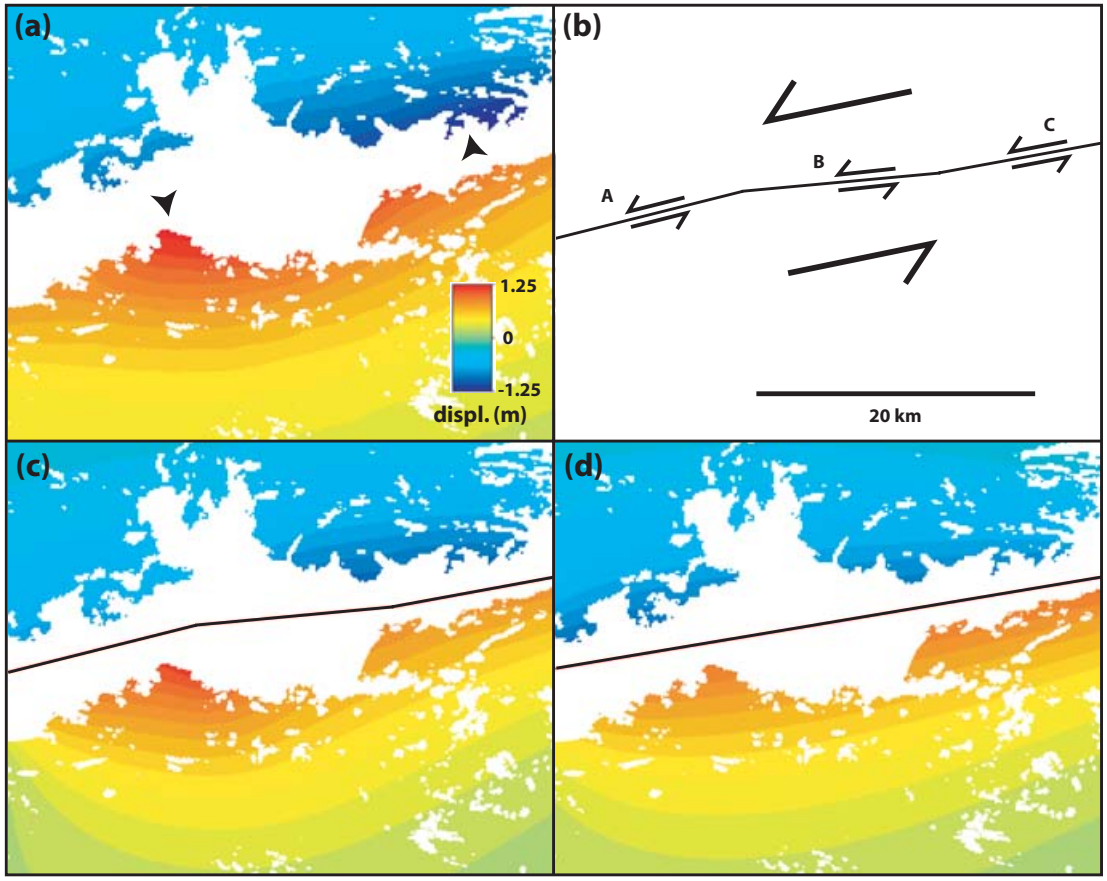

Figure 12. Recreating the asymmetry in the Manyi interferogram. (a) Unwrapped interferogram data. The black arrowheads indicate the location of the loci of maximum motion of the south and north sides of the fault, which are offset by ∼20 km in a right-lateral sense. The colour palette is stepped so that the approximate orientations of the interference fringes can be estimated. (b) Simple right-jog configuration of fault segments based upon the mapped trace of the fault in this area (segments 4, 5 and 6 from Fig. 6). (c) Forward model based upon the configuration of faults in (b). The main features of the real interferogram, such as the offset of the loci of peak motion and the curvature of lines of equal displacement, are reproduced with some success by this simple uniform-slip linear elastic model (further details given in the text). (d) Forward model of uniform slip on a straight fault plane with a linear elastic rheology, as used by Peltzer *et al.* (1999) to compare with the non-linear elastic case. Here, the pattern of maximum displacements is approximately symmetric about the fault.

the other two dip at 80° to the north. Fig. 12c shows the synthetic interferogram calculated for this fault geometry. The locations of the loci of maximum displacement either side of the fault are offset by over 15 km, and are close to their locations in the observed interferogram (Fig. 12a). The shape of the displacement pattern also mimics that of the real data, in terms of the curvature of the lines of equal displacement, suggesting that the observed asymmetry in the data could be explicable in terms of a simple linear elastic model. This is compared with a model based upon a straight vertical fault, with the same slip, depth and rake as the three segment model; the pattern of displacements in this case is symmetrical (Fig. 12d), with the loci of maximum displacement either side of the fault opposite each other across the fault. This model is a poor match to the real data, and demonstrates that vertical straight fault models, similar to those used by Peltzer *et al.* (1999) to test the linear elastic case, will not reproduce the observed displacement pattern in this region, and should not be used to evaluate the relative merits of the competing rheological models.

A bending fault model with a reversal of dip can explain both the asymmetry of the maxima of line-of-sight displacement of both sides of the fault, and also provides the best fit to the entire displacement field. Such dip-reversing strike-slip fault geometries have been obtained in sandbox models of double restraining bends (e.g. McClay & Bonora 2001), and as such are mechanically plausible. As the inferred dip reversal occurs at the location of a restraining double fault bend, coincident with a pressure ridge (Section 3.1.3; Figs 4e and f), we believe that the model is also geologically plausible. There are other independent observations which may support this conclusion. The hypocentre of the earthquake, located using the best regional seismic velocity models by Steck *et al.* (2001), is close to this reversal in dip, near the junction of the fourth and fifth fault segments (Fig. 6). This is reminiscent of other large earthquakes, such as the M_w 6.9 Kobe (1995) and the great M_w 7.8 San Francisco earthquake (1906), which are believed to have nucleated in the stepovers between inward-dipping fault segments (Jachens & Zoback 1999; Zoback 2003). Although the geometry is not exactly identical in this case – the fault segments here dip outwards rather than inwards – it is likely that such a configuration of faults would result in a concentration of stress that would promote failure in the region of the junction of the faults.

5.3 Post seismic deformation and coseismic moment estimates

In a related study, we have observed significant post-seismic deformation in SAR interferograms of the Manyi area in the three years following the 1997 earthquake (Ryder *et al.*, 2007). Although the mechanism of the deformation cannot be unequivocally identified, it can be shown that afterslip consistent with the coseismic stress change on a deeper portion of the Manyi fault is a plausible candidate, and that the most rapid post-seismic deformation occurs in the immediate aftermath of the earthquake. Each of the three coseismic interferograms will have sampled a portion of this early post-seismic deformation, with the first useable post-earthquake image acquisition occurring 8, 24 and 40 days after the earthquake on tracks 076, 305 and 033, respectively. It is therefore, likely that some proportion of the post-seismic deformation signal will have been mapped into our coseismic slip models, on the lower portions of the fault.

A comparison of the moment estimates derived from our variable slip modelling of the InSAR displacements (Table 5) with seismically derived moment estimates (Table 1) is consistent with the notion that the geodetic models may overestimate the coseismic moment. In the absence of continuous GPS observations that have been used to correct coseismic models generated from InSAR data (e.g. Cakir *et al.* 2003), careful comparison between, and joint inversion of, the InSAR data and seismic waveform data have the most potential as means to quantify the proportion of these coseismic moment estimates that is due to rapid post-seismic deformation, and that due to uncertainties in the model.

ACKNOWLEDGMENTS

This work was supported by the Natural Environment Research Council (NERC) through the Centre for the Observation and Modelling of Earthquakes and Tectonics (COMET), as well as through a research studentship to GJF. GJF also acknowledges support from a Hertford College Senior Scholarship, and a Lindemann Trust Postdoctoral Fellowship. TJW is supported by a Royal Society Research Fellowship. Thanks to David Robinson for providing aftershock relocations, Isabelle Ryder for helpful discussions, and to Wayne Thatcher and one anonymous reviewer for thorough and constructive reviews and comments that have helped to improve the manuscript. All ERS–SAR data is copyrighted by the European Space Agency, and was acquired under project AOE-621. Some of the figures were made using the public domain Generic Mapping Tools (Wessel & Smith 1998).

REFERENCES

Antolik, M., Abercrombie, R.E. & Ekstrom, G., 2004. The 14 November Kokoxili (Kunlunshan), Tibet, earthquake: rupture transfer through a large extensional stepover, *Bull. seism. Soc. Am.*, **94,** 1173–1194.

Bro, R. & De Jong, S., 1997. A fast non-negativity-constrained least squares algorithm, *J. Chemometrics*, **11,** 392–401.

Cakir, Z., de Chabalier, J.-B., Armijo, R., Meyer, B., Barka, A. & Peltzer, G., 2003. Coseismic and early post-seismic slip associated with the 1999 Izmit earthquake (Turkey), from sar interferometry and tectonic field observations, *Geophys. J. Int.*, **155,** 93–110.

Clarke, P., Paradissis, D., Briole, P., England, P., Parsons, B., Billiris, H., Veis, G. & Ruegg, J.-C., 1997. Geodetic investigation of the 13 May 1995 Kozani—Grevena (Greece) earthquake, *Geophys. Res. Lett.*, **24**(6), 707–710.

Dewey, J.W., 1971. Seismicity studies with the method of joint hypocenter determination, *PhD thesis*, University of California, Berkeley, USA.

Du, Y., Aydin, A. & Segall, P., 1992. Comparison of various inversion techniques as applied to the determination of a geophysical deformation model for the 1983 Borah Peak earthquake, *Bull. seism. Soc. Am.*, **82,** 1840–1866.

Farr, T. & Kobrick, M., 2000. Shuttle Radar Topography Mission produces a wealth of data, *EOS, Trans. Am. geophys. Un.*, **81,** 583–585.

Fialko, Y., Simons, M. & Agnew, D., 2001. The complete (3-D) surface displacement field in the epicentral area of the 1999 M_w 7.1 Hector Mine earthquake, California, from space geodetic observations, *Geophys. Res. Lett.*, **28**(16), 3063–3066.

Fielding, E.J., Talebian, M., Rosen, P.A., Nazari, H., Jackson, J.A., Ghorashi, M. & Walker, R., 2005. Surface ruptures and building damage of the 2003 Bam, Iran earthquake mapped by satellite SAR interferometric correlation, *J. geophys. Res.*, **110,** B03302, doi:10.1029/2004JB003299.

Fukahata, Y., Funning, G.J., Yagi, Y. & Parsons, B., 2005. Joint inversion of InSAR and teleseismic broadband waveform data using ABIC: application to the 1997 Manyi, Tibet earthquake, *EOS, Trans. Am. geophys. Un.*, **86**(47), Abstract G51C–0841.

Funning, G.J., 2005. Source parameters of large shallow earthquakes in the Alpine-Himalayan belt from InSAR and waveform modelling, *D.Phil. thesis*, University of Oxford, Oxford, UK.

Funning, G.J., Parsons, B., Wright, T.J., Jackson, J.A. & Fielding, E.J., 2005. Surface displacements and source parameters of the 2003 Bam (Iran) earthquake from Envisat advanced synthetic aperture radar imagery, *J. geophys. Res.*, **110**(B09406), doi:10.1029/2004JB003338.

Jachens, R.C. & Zoback, M.L., 1999. The San Andreas fault in the San Francisco Bay region, California: structure and kinematics of a young plate boundary, *Int. Geol. Rev.*, **41,** 191–205.

Jónsson, S., Zebker, H., Segall, P. & Amelung, F., 2002. Fault slip distribution of the 1999 Mw 7.1 Hector Mine earthquake, California, estimated from satellite radar and GPS measurements, *Bull. seism. Soc. Am.*, **92**(4), 1377–1389.

Lasserre, C., Peltzer, G., Crampé, F., Klinger, Y., der Woerd, J.V. & Tapponnier, P., 2005. Coeismic deformation of the $M_w = 7.8$ Kokoxili earthquake in Tibet measured by synthetic aperture radar interferometry, *J. geophys. Res.*, **110**(B12), B12408, doi:10.1029/2004JB003500.

McClay, K. & Bonora, M., 2001. Analog models of restraining stepovers in strike-slip fault systems, *Am. Assoc. Petrol. Geol. Bull.*, **85,** 233–260.

Michel, R., Avouac, J.-P. & Taboury, J., 1999. Measuring ground displacements from SAR amplitude images: application to the Landers earthquake, *Geophys. Res. Lett.*, **26,** 875–878.

Molnar, P. & Chen, W.-P., 1983. Focal depths and fault plane solutions of earthquakes under the Tibetan plateau, *J. geophys. Res.*, **99,** 1180–1196.

Okada, Y., 1985. Surface deformation due to shear and tensile faults in a half-space, *Bull. seism. Soc. Am.*, **75**(4), 1135–1154.

Peltzer, G., Crampé, F. & King, G., 1999. Evidence of nonlinear elasticity of the crust from the Mw 7.6 Manyi (Tibet) earthquake, *Science*, **286,** 272–276.

Rosen, P.A., Hensley, S., Joughin, I.R., Li, F.K., Madsen, S.N., Rodriguez, E. & Goldstein, R.M., 2000. Synthetic aperture radar interferometry, *Proceedings of the IEEE*, **88**(3), 333–382.

Rosen, P.A., Hensley, S., Peltzer, G. & Simons, M., 2004. Updated Repeat Orbit Interferometry package released, *EOS, Trans. Am. geophys. Un.*, **85**(5), 35.

Ryder, I., Parsons, B., Wright, T.J. & Funning, G.J., 2007. Post-seismic motion following the 1997 Manyi (Tibet) earthquake: InSAR observations and modelling, *Geophys. J. Int.*, doi:10.1111/j.1365-246X.2006.03312.x.

Scharroo, R. & Visser, P., 1998. Precise orbit determination and gravity field improvement for the ERS satellites, *J. geophys. Res.*, **103**(C4), 8113–8127.

Simons, M., Fialko, Y. & Rivera, L., 2002. Coseismic deformation from the 1999 M_w 7.1 Hector Mine, California earthquake as inferred from InSAR and GPS observations, *Bull. seism. Soc. Am.*, **92,** 1390–1402.

Steck, L.K., Velasco, A.A., Cogbill, A.H. & Patton, H.J., 2001. Improving regional seismic event location in China, *Pure appl. Geophys.*, **36,** 192–205.

Talebian, M. *et al.,* 2004. The 2003 Bam (Iran) earthquake: rupture of a blind strike-slip fault, *Geophys. Res. Lett.*, **31,** L11611, doi:10.1029/2004GL020058.

Tapponnier, P. & Molnar, P., 1977. Active faulting and tectonics in China, *J. geophys. Res.*, **82,** 2905–2930.

Van der Woerd, J. *et al.,* 1998. Holocene left-slip rate determined by cosmogenic surface dating on the Xidatan segment of the Kunlun fault (Qinghai, China), *Geology*, **26,** 695–698.

Van der Woerd, J. *et al.,* 2002. Uniform postglacial slip-rate along the central 600 km of the Kunlun Fault (Tibet) from Al-26, Be-10, and C-14 dating of riser offsets and climatic origin of the regional morphology, *Geophys. J. Int.*, **148,** 356–388.

Velasco, A.A., Ammon, C.J. & Beck, S.L., 2000. Broadband source modeling of the November 8, 1997, Tibet ($M_w = 7.5$) earthquake and its tectonic implications, *J. geophys. Res.*, **105,** 28 065–28 080.

Wessel, P. & Smith, W.H.F., 1998. New, improved version of generic mapping tools released, *EOS, Trans. Am. geophys. Un.*, **79,** 579.

Wright, T.J., Parsons, B., Jackson, J., Haynes, M., Fielding, E., England, P. & Clarke, P., 1999. Source parameters of the 1 October 1995 Dinar (Turkey) earthquake from SAR interferometry and seismic bodywave modelling, *Earth planet. Sci. Lett.*, **172,** 23–37.

Wright, T.J., Lu, Z. & Wicks, C., 2003. Source model for the M_w 6.7, 23 October 2002, Nenana Mountain Earthquake (Alaska) from InSAR, *Geophys. Res. Lett.*, **30**(18), doi:10.1029/2003GL018014.

Wright, T.J., Lu, Z. & Wicks, C., 2004. Constraining the slip distribution and fault geometry of the M_w 7.9, 3 November 3 2002, Denali Fault Earthquake with InSAR and GPS, *Bull. seism. Soc. Am.*, **94**(6B), S175–S189.

Xu, X., Chen, W., Ma, W., Yu, G. & Chen, G., 2002. Surface rupture of the Kunlunshan earthquake (M 8.1), northern Tibetan plateau, China, *Seismol. Res. Lett.*, **73,** 884–892.

Yeats, R.S., Seih, K. & Allen, C.R., 1997. *The Geology of Earthquakes*, Oxford University Press, Oxford.

Zoback, M.L., 2003. Relationship between mapped fault stepovers and earthquake fault planes at depth, *EOS, Trans. Am. geophys. Un.*, **86,** Fall Meet. Suppl. Abstract T12E–03.

APPENDIX A: DETAILS OF VARIABLE SLIP MODELLING

The approach to variable slip modelling taken in this study is broadly similar to those used in our previous space geodetic studies of earthquakes (e.g. Wright *et al.* 2004; Funning *et al.* 2005), to which we refer the reader for a more detailed treatment of the mathematics. We simultaneously solve for slip (either a single component of slip, if a fixed rake is assumed, or two components of slip if variable slip is allowed) on an array of rectangular fault patches, a static shift in displacement for each interferogram data set (to account for the zero-level ambiguity in each data set), and gradients of displacement in the N–S and E–W direction (to account for errors in the orbital corrections used in the InSAR processing), all of which are linearly related to the observed data. Modelled values of slip are subject to a finite-difference Laplacian smoothing criterion and a positivity constraint, in order to prevent large oscillations in slip, which can imply localized strain gradients in excess of the known mechanical strength of crustal rocks, and physically unlikely retrograde slip, respectively. Given our lack of knowledge of shallow crustal structure and seismic velocities in the source region, a uniform linear elastic rheology, with Lamé elastic parameters $\lambda = 32.3$ and $\mu = 34.3$ GPa, is assumed for all elastic dislocation models in this study.

A1 The influence of smoothing

The relative weighting of the observations and smoothing as constraints on the model solution is controlled by a smoothing parameter, κ. Increased values of κ represent an increase in the influence of smoothing on the result, and vice versa. The value of κ assumed has a strong influence on the form, amplitude and resolution of the model obtained (e.g. Funning *et al.* 2005), and therefore, a clear rationale must be given for the choice of κ in a solution of this type.

In this study, we adopt the method of Jónsson *et al.* (2002), whereby the rms misfit between modelled and observed values of displacement is plotted against 'solution roughness', a dimensionless quantity equivalent to the average gradient of slip on the fault plane, for a series of values of κ. Fig. A1 shows plots of misfit against solution roughness for the fixed rake and variable rake cases. There is a reciprocal relationship between the two quantities; the value of κ that we select in each case – 850 for the fixed rake model, 700 for the variable rake model – corresponds to a compromise between them. In effect, the values selected give the best-fitting smooth model solution in each case.

A2 Model uncertainties

Uncertainties in the modelled slip values that we obtain are estimated with a Monte Carlo technique using realistically perturbed data. We

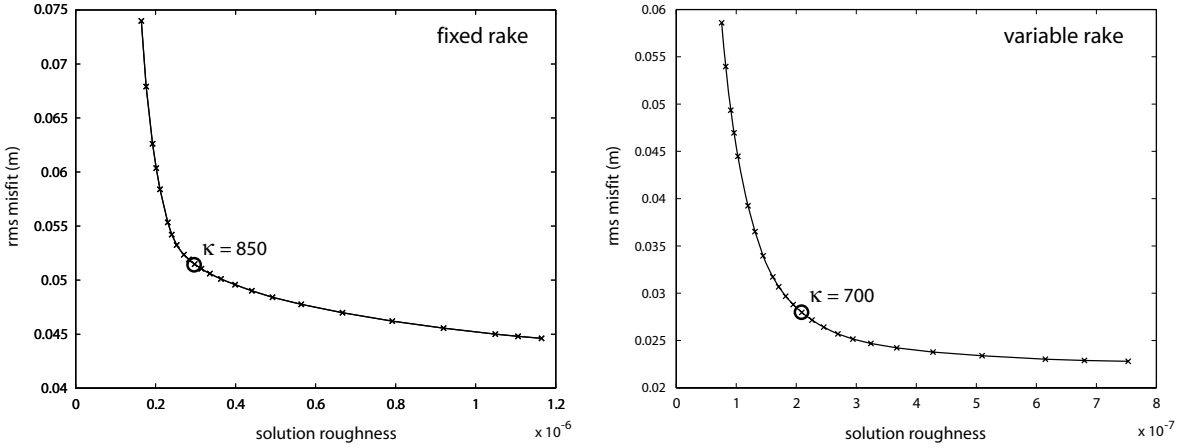

Figure A1. Selection of smoothing parameter (κ) for variable slip models. Root-mean-square (rms) misfit is plotted against solution roughness (e.g. Jónsson *et al.* 2002) for a set of model runs with different values of κ. The values selected (850 for the fixed rake inversion, 700 for the variable rake inversion) represent the best compromise between the smoothness of the solution and its ability to fit the data.

generate 100 sets of random synthetic correlated noise with the statistical properties of the residual phase in the far-field (>50 km from the fault, in this case), following the subtraction of a uniform-slip model (Section 4.3.2, Fig. 9) and best-fitting plane from the data. These are then added to the resampled interferogram data sets to create 100 perturbed data sets, each of which is inverted as described above. The standard deviation of the model slip values obtained for each fault patch in this way is used as a measure of the uncertainty of our slip estimate for that patch. More detailed descriptions of the methodology are given elsewhere (e.g. Wright *et al.* 2003; Funning *et al.* 2005; Wright *et al.*, in preparation).

A3 Model resolution

The resolution matrix, **R**, of a given fault slip model is given by the relation:

$$\mathbf{R} = [\mathbf{A}^T\mathbf{A} + \kappa^2\mathbf{S}^T\mathbf{S}]^{-1}\mathbf{A}^T\mathbf{A}, \quad \text{(A1)}$$

where **A** is the kernel matrix relating model slip to measured ground displacement, **S** is the finite difference Laplacian operator used to smooth the data, and κ is the smoothing parameter, as above. The elements of **R** range in value between 0 and 1 with the elements in a single column summing to 1, each column representing a different fault patch in the model. If slip is perfectly resolved on a given patch, then the corresponding column in **R** will have a value of 1 at the leading diagonal position, and zeros elsewhere. If the model is underdetermined, there will be off-diagonal terms, the number and size of which reflect the degree to which slip on that patch is averaged with that of its neighbours in the model (e.g. Du *et al.* 1992).

This property of the resolution matrix can be used to estimate the spatial resolution at the location of any fault patch in the model. To demonstrate this, we project the columns of **R** (also known as 'resolution kernels') for 12 example fault patches at different depths and along-strike locations onto the fault plane for both the fixed rake case and variable rake case. We show the fixed rake case as an example (Fig. A2). The spatial extent of the contoured resolution kernels is used as a proxy for the scale of the smallest resolvable feature at each example fault patch; an area of the fault where resolving power is high will have high kernel values tightly clustered in a few neighbouring patches, an area with poor resolution will have low values distributed between many patches. A peak resolution of ~5 km, in both horizontal and vertical dimentsions, is obtained close to the centre of the fault in the upper layer of fault patches (Fig. A2g). In the central area of the fault, between 50 and 140 km along-strike, the horizontal resolution does not degrade substantially away from this peak

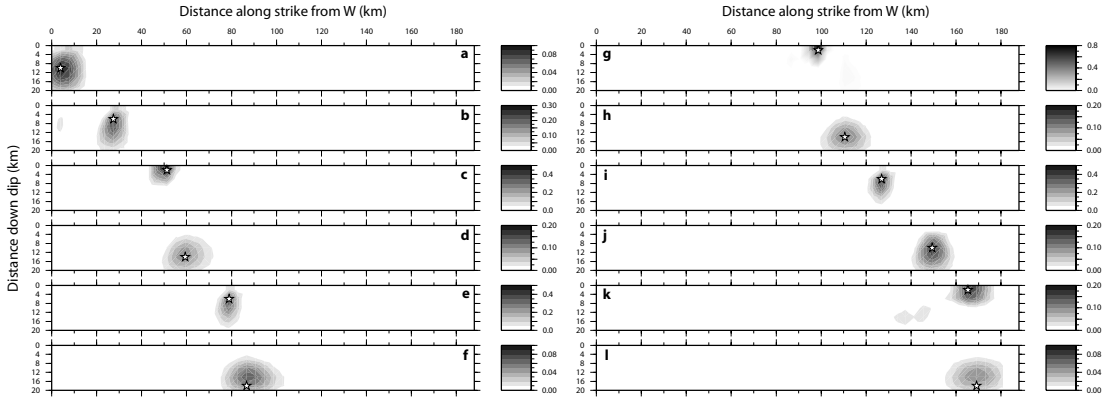

Figure A2. Resolution kernels for the fixed rake variable slip model. The columns of the resolution matrix from 12 sample locations are projected onto the fault and contoured. The fault elements represented by each of the kernels are indicated by white stars. The extent of the area covered by each resolution kernel is an indication of the size of a slip feature that can be resolved in the model. Further description is given in the main text.

in the upper 8 km of the fault, where most of the peak fault slip occurs (Fig. 10h), although the vertical resolution increases to ∼10 km in the second layer of fault patches (4–8 km depth, e.g. Fig. A2e, i). Away from this central, upper fault region, both horizontal and vertical resolution degrade significantly, with the lowest horizontal resolution of ∼20 km occurring at the base of the fault (e.g. Fig. A2f, l) and the lowest vertical resolution, of ∼18 km, at the western end of the fault (Fig. A2a). Resolution is, therefore, good in the areas where the greatest slip occurs, and therefore, we believe that the features that we interpret in those areas are adequately resolved.

For the variable rake case, the pattern of resolution kernels is very similar and the same general conclusions can be drawn about the resolution of most of the slip features, with perhaps the exception of the deep slip at fault segment 6 (12–20 km depth, 120–128 km along-strike), which occurs in a portion of the fault where the resolution kernels are likely to be widely dispersed (Figs 11h, A2f,l), and is thus poorly resolved. Overall, resolution is marginally degraded (by up to a few km) with respect to the fixed rake case, due to the estimation of double the number of slip parameters. As may also be expected, dip-slip fault displacements are better resolved than strike-slip, given that InSAR measurements with ERS satellite data are approximately three times more sensitive to vertical deformation than horizontal.

SUPPLEMENTARY MATERIAL

The following supplementary material is available for this article:

Table S1. Vertices of Manyi fault model elements.
Table S2. Modelled values of fault slip and rake.

This material is available as part of the online article from: http://www.blackwell-synergy.com/doi/abs/10.1111/j.1365-246X.2006.03318.x

(This link will take you to the article abstract.)
Please note: Blackwell Publishing are not responsible for the content or functionality of any supplementary materials supplied by the authors. Any queries (other than missing material) should be directed to the corresponding author for the article.